



**HAL**  
open science

# **In silico experiments of intimal hyperplasia development: disendothelization in an axisymmetric idealized artery**

Jérôme Jansen, Xavier Escriva, Fabien Godeferd, Patrick Feugier

## ► **To cite this version:**

Jérôme Jansen, Xavier Escriva, Fabien Godeferd, Patrick Feugier. In silico experiments of intimal hyperplasia development: disendothelization in an axisymmetric idealized artery. *Biomechanics and Modeling in Mechanobiology*, 2023, 10.1007/s10237-023-01720-7 . hal-04085178v1

**HAL Id: hal-04085178**

**<https://hal.science/hal-04085178v1>**

Submitted on 28 Apr 2023 (v1), last revised 18 May 2023 (v2)

**HAL** is a multi-disciplinary open access archive for the deposit and dissemination of scientific research documents, whether they are published or not. The documents may come from teaching and research institutions in France or abroad, or from public or private research centers.

L'archive ouverte pluridisciplinaire **HAL**, est destinée au dépôt et à la diffusion de documents scientifiques de niveau recherche, publiés ou non, émanant des établissements d'enseignement et de recherche français ou étrangers, des laboratoires publics ou privés.

# *In silico* experiments of intimal hyperplasia development : disendothelization in an axisymmetric idealized artery

Jérôme Jansen<sup>1\*</sup>, Xavier Escriva<sup>1</sup>, Fabien Godeferd<sup>1</sup> and Patrick Feugier<sup>2</sup>

<sup>1\*</sup>Laboratoire de Mécanique des Fluides et d'Acoustique, CNRS, Univ de Lyon, Ecole Centrale de Lyon, 36 Av. Guy de Collongue, Ecully, 69134, France.

<sup>2</sup>Service de Chirurgie Vasculaire et Endovasculaire, LYVES Groupement Hospitalo-Universitaire Lyon Sud, Université Claude Bernard Lyon 1 Lyon, Villeurbanne, 69100, France.

\*Corresponding author(s). E-mail(s): [jrme.jansen@gmail.com](mailto:jrme.jansen@gmail.com);

Contributing authors: [xavier.escriva@ec-lyon.fr](mailto:xavier.escriva@ec-lyon.fr); [fabien.godeferd@ec-lyon.fr](mailto:fabien.godeferd@ec-lyon.fr);  
[patrickfeugier@hotmail.fr](mailto:patrickfeugier@hotmail.fr);

## Abstract

We use *in silico* experiments to study the role of the hemodynamics and of the type of disendothelization on the physiopathology of intimal hyperplasia. We apply a multiscale bio-chemo-mechanical model of intimal hyperplasia on an idealized axisymmetric artery that suffers two kinds of disendothelizations. The model predicts the spatio-temporal evolution of the lesions development, initially localized at the site of damages, and after few days displaced downstream of the damaged zones, these two stages being observed whatever the kind of damage. Considering macroscopic quantities, the model sensitivity to pathology-protective and pathology-promoting zones is qualitatively consistent with experimental findings. The simulated pathological evolutions demonstrate the central role of two parameters: (a) the initial damage shape on the morphology of the incipient stenosis, and (b) the local wall shear stresses on the overall spatio-temporal dynamics of the lesion.

**Keywords:** Intimal hyperplasia, Growth and Remodelling, Hemodynamics, Wall Shear Stress, Multiscale modeling

1	<b>Contents</b>	10	3.1	Macroscopic lesion evolution . . . .	9
2	<b>1 Introduction</b>	2	3.1.1	Detection of remodelling criteria . . . . .	9
3	<b>2 Methods</b>	3	3.1.2	Evolution of the luminal radius . . . . .	11
4	2.1 Hemodynamics modelling . . . . .	3	3.1.3	Comparison between 1D and 2D geometries . . . . .	11
5	2.2 Intimal hyperplasia modelling . . . . .	5	3.1.4	Arterial generations: CFD resolutions and wall shear stress stimuli . . . . .	13
6	2.3 Coupling methods in a bidimensional domain . . . . .	6			
7	2.4 Disendothelization models . . . . .	7			
8		7			
9	<b>3 Results and Discussions</b>	9			

20	3.2	Spatio-temporal dynamics of tissues growth . . . . .	16
21	3.2.1	Endothelium regeneration . . . . .	16
22	3.2.2	Functional properties of vSMCs . . . . .	16
23	3.2.3	Dynamics of sSMCs . . . . .	18
24	3.2.4	Composition of lesions . . . . .	19
25			
26			

27	4	Conclusion and perspectives	22
----	---	-----------------------------	----

28	5	Acknowledgments	23
----	---	-----------------	----

29	A	Reproducibility data, computational costs and sensitivity analysis	23
----	---	--	----

30	B	Mesh convergence study	23
----	---	------------------------	----

## Declarations

**Funding :** No funding was received to assist with the preparation of this manuscript.

**Competing interests :** The authors have no conflicts of interest to declare that are relevant to the content of this article.

**Code availability :** All simulation has been achieved with in-house Python packages <https://gitlab.com/jrme.jansen/pytg/>. Python codes used in this study will be available after publication on the gitlab repository.

**Authors' contributions :** X. Escriva and P. Feugier set up the relevant framework for tackling the modelling of the physiological-mechanical pathology. J. Jansen developed the model and code in axisymmetric configuration, carried out simulations and wrote the manuscript. F. Godefert, X. Escriva and P. Feugier participated in the discussion of the results. J. Jansen and F. Godefert wrote the first draft of manuscript.

**Ethics approval :** This article does not present research with ethical considerations.

**Consent to participate :** All the authors consented to participate in this study.

**Consent for publication :** All authors proof-read and consent for the publication of the manuscript.

# 1 Introduction

Intimal hyperplasia (IH) is a thickening of the intima layer of blood vessel resulting from a tissue growth. Subbotin [18] define an IH lesion as “any cells that form a multi-layer compartment internally to the elastic membrane of the arterial wall and express alpha-smooth-muscle actin, permanently or transitionally”. Macroscopically, IH causes a reduction in the luminal section of a blood vessel which can lead to its obstruction. At the tissue level, this pathology results from a cascade of biological processes causing a structural rearrangement of the intimal layers of the vascular wall.

Hemodynamics is known to modulate the development of intimal hyperplasia. Although the relationship between vascular adaptation and local hemodynamics has been described for over a century [2], it was in the 1980s that evidence for a relationship between vascular disease development and hemodynamics was obtained [8]. We refer to the review of Peiffer et al. [15] for a detailed history of the influence of hemodynamics on pathological development. Nowadays, the concept that disturbed local hemodynamics is a key factor in the development of vascular lesions — with an inverse correlation between lesion thickness and wall shear stress — is widely accepted [15, 20]. However, Peiffer et al. [15] noticed that “the evidence for it (theory) is less clear-cut than might at first appear”.

Despite several decades of high-level medicine research field to understand and treat the onset of intimal hyperplasia through animal models, *in vitro* and *in vivo* studies, much remains to be understood [18]. As “No new conceptual ideas seem to have arisen during the past 50–60 years of study of arterial neointimal formation” [18], we observe in literature more and more *in silico* studies which propose mathematical model of multiple vascular pathologies to test hypotheses or to address unresolved questions about pathologies. Escuer et al. [7] study the process of restenosis following the implantation of a stent by a set of partial differential equation of reaction–diffusion type to model the evolution of the lesion. In the context of tissue-engineered vascular grafts, Khosravi et al. [13] propose a mathematical model of the development of grafts with bio-chemo-mechanical

equations. Several studies have proposed mathematical models to predict the spatio-temporal development of various vascular pathologies by considering the coupling with blood flow : Cilla et al. [4], Calvez et al. [1] and Corti et al. [5] for atherosclerosis, Goodman et al. [10] and Donadoni et al. [6] for intimal hyperplasia.

Starting from the study of Donadoni et al. [6], we introduced in Jansen et al. [12] a novel multiscale and multiphysics model of intimal hyperplasia in a bio-chemo-mechanical framework. Our model considers the interactions between hemodynamics, cellular dynamics and biochemistry in a compartmental approach. This mathematical model is based on kinetic differential equations for key vascular species (cellular and non cellular populations) and growth factors. The model was validated on a monodimensional test-case [12].

In the present study, we strictly apply our modelling [12] in a novel geometrical configuration. The main novelty of this work is about the generalization of methods applied to our compartmental modelling into a tridimensional arterial configuration. We present a methodology to manage arterial remodeling in tridimensional configuration which consider a novel algorithm of automatic arterial remodelling with time- and space-dependent detection of remodeling criteria. We consider an application of our modelling in an idealized axisymmetric artery undergoing two different kinds of initial endothelial damage, and we follow the spatio-temporal evolution of the lesions predicted by our model. The aim of the present paper is therefore threefold: (a) we evaluate the response of the model in pathology-protective and pathology-promoting zones described in the literature [15]; (b) we compare the results of one- and tri-dimensional configurations to assess the influence of the geometrical configuration; (c) we explore the influence of the initial endothelial injury on the development of the lesion.

The article is organized as follows. In section 2, we present methods used for computing the model of IH in an axisymmetric idealized artery: in section 2.1, we present the hemodynamics assumptions, equations and numerical methods; in section 2.2, we shortly introduce the model of IH; section 2.3 is devoted to coupling methods in an axisymmetric configuration; finally in section 2.4 we initialize the physiological-damage conditions by defining two types of endothelial damages.

Section 3 is devoted to the results and discussion of the spatio-temporal evolutions of lesions. Section 4 reports our main conclusions.

## 2 Methods

### 2.1 Hemodynamics modelling

In the luminal domain  $\Omega_1$  (see left Figure 1), the blood flow is assumed to be a stationary laminar flow in a rigid duct, whose dynamics is that of an incompressible Newtonian fluid. Hemodynamics is therefore governed by the Navier–Stokes equations

$$\frac{\partial \mathbf{u}}{\partial t} + (\mathbf{u} \cdot \nabla) \mathbf{u} = -\frac{1}{\rho} \nabla p + \nu \Delta \mathbf{u} \quad \text{in } \Omega_1, \quad (1a)$$

$$\nabla \cdot \mathbf{u} = 0 \quad \text{in } \Omega_1, \quad (1b)$$

where  $\mathbf{u}$  is the velocity vector,  $p$  the pressure,  $\rho$  the constant blood density,  $\nu$  the constant kinematic viscosity and  $\mu = \rho\nu$  the constant dynamical viscosity.

The hemodynamics is characterized by the Reynolds number  $Re = (2Q_v) / (\pi R_1 \nu)$  based on the volumic blood flow rate  $Q_v$  and the luminal radius  $R_1$ . As in Jansen et al. [12], we choose  $Re_0 = 300$  at  $t_0$ , and the initial luminal domain is a straight artery of uniform radius  $R_0$  and of length  $L = 45R_0$ . Throughout the IH lesion development, we assume axisymmetric morphological changes of  $\Omega_t$ , so that hemodynamical variables  $(\mathbf{u}, p)$  are only radially- and axially-dependent. Three-dimensional hemodynamically simulations are therefore done in a wedge geometry, which is used to solve equations in the azimuthal plane, assuming axisymmetry of the problem.

The boundary conditions (BCs) applied at each surface of the luminal domain are

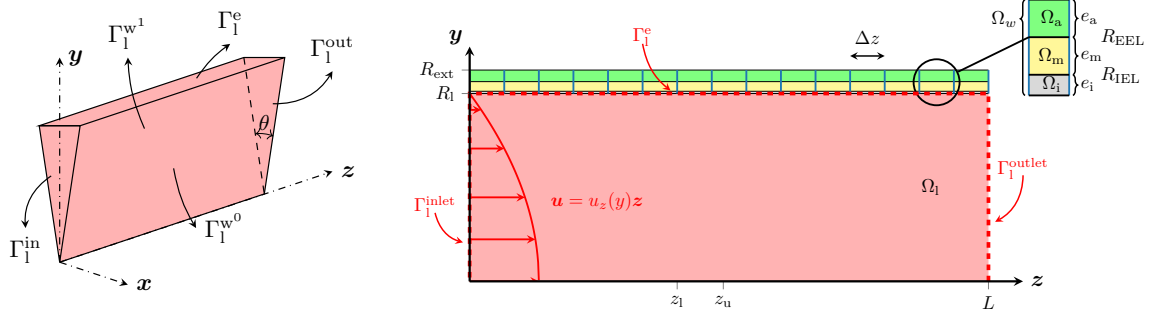


**Fig. 1:** (Left) Initial luminal domain of a straight axisymmetric artery modelled by a 3D wedge geometry, with wedge angle  $\theta = 3^\circ$ .  $\Omega_1$  is the luminal domain delimited by four surfaces: inlet  $\Gamma_1^{\text{in}}$ , endothelium wall  $\Gamma_1^e$ , outlet  $\Gamma_1^{\text{out}}$  and wedge sides  $\Gamma_1^{w,0,1}$ . (Right) Cut of the considered idealized artery in the symmetry plane  $(z, y)$  with  $z$  and  $y$  respectively the longitudinal and radial directions. The three boundary surfaces are shown in dashed lines. The arterial segment of length  $L$  initially suffers a damage of endothelium between  $z_1$  and  $z_u$ . The endothelial surface  $\Gamma_1^e$  is the interface between lumen and arterial wall at  $r = R_1$ , the luminal radius. The blow up shows an arterial wall compartment with  $\Omega_i$  the intima layer of thickness  $e_i$  between  $R_1$  and  $R_{\text{IEL}}$  (radius of internal elastic lamina),  $\Omega_m$  the media layer of thickness  $e_m$  between  $R_{\text{IEL}}$  and  $R_{\text{EEL}}$  (radius of external elastic lamina),  $\Omega_a$  the adventitial layer of thickness  $e_a$  between  $R_{\text{EEL}}$  and  $R_{\text{ext}}$  (the external radius of the artery). The whole arterial wall domain is noted  $\Omega_w$ . A uniform parietal mesh is shown with compartments of length  $\Delta z$  (blue vertical lines).

$$\begin{aligned} \text{at } \Gamma_1^{\text{in}} : & \begin{cases} \mathbf{u} = u_{\text{max}} (1 - (y/R_{1,\text{in}})^2) \mathbf{z}, \\ \nabla p \cdot \mathbf{n} = 0, \end{cases} \\ \text{at } \Gamma_1^{\text{out}} : & \begin{cases} (\nabla \mathbf{u}) \cdot \mathbf{n} = \mathbf{0}, \\ p = 0, \end{cases} \end{aligned}$$

$$\text{at } \Gamma_1^e : \begin{cases} \mathbf{u} = \mathbf{0}, \\ \nabla p \cdot \mathbf{n} = 0, \end{cases} \quad (2c)$$

$$\text{at } \Gamma_1^{w,0,1} : \begin{cases} (\nabla \mathbf{u}) \cdot \mathbf{n} = \mathbf{0}, \\ \nabla p \cdot \mathbf{n} = 0, \end{cases} \quad (2d)$$

210 surface (2c), a no-slip condition is assumed, *i.e.*  
 211 zero velocity relative to the wall which is assumed  
 212 (2a) rigid in hemodynamical timescale [12]. Finally,  
 213 zero pressure gradient is imposed at wall.

214 (2b) The wall shear stress (WSS) vector is  $\boldsymbol{\tau}_w$  and  
 215 of magnitude  $\tau_w$ :

$$\boldsymbol{\tau}_w = \mu (\nabla \mathbf{u} + \nabla \mathbf{u}^T) \cdot \mathbf{n} \quad \text{in } \Omega_e, \quad (3a)$$

$$\tau_w = |\boldsymbol{\tau}_w| \quad \text{in } \Omega_e. \quad (3b)$$

It represents the tangential friction stress exercised by blood on the luminal wall. (3b) is used in the present model to account for hemodynamics in the IH model.

CFD computations use the OpenFOAM code version 5.0 [19], a C++ object oriented library widely used in research and industry. It is open source, efficient, flexible, and easily updatable. OpenFOAM implements the Finite Volume Method (FVM) on cartesian and colocated grids.

Under axisymmetric assumption, the computational luminal domain is a thin wedge of angle  $\theta$  and of one cell thick along the circumferential direction [19] (shown in left Figure 1).

197

198

199

200

201

202

203

204

205

206

207

208

209

216

217

218

219

220

221

222

223

224

225

226

227

228

229

We use the Semi-Implicit Method for Pressure-Linked Equations (SIMPLE) solver proposed by default in OpenFOAM [19] to solve equations (1) with boundary conditions (2). The parameters chosen for our OpenFOAM simulations are listed in Table 1 for boundary conditions and Table 2 for Navier–Stokes equations discretization.

For the first hemodynamical generation in the geometry of Figure 1, we initialize velocity and pressure fields as a Poiseuille flow. The initial guess velocity profile is in equation (2a) and initial pressure field is  $p(z) = -Gz + p_{\text{in}}$ , with  $G = -(p_{\text{out}} - p_{\text{in}})/L$  the pressure gradient and  $L$  the total length of the artery.

The 3D wedge mesh is built using Gmsh [9]. It is a structured mesh composed of prisms along the axis of symmetry of revolution and hexahedral elements with non-uniform grading in radial direction, as well as at inlet and outlet. The cells are also denser near wall for accurate evaluation of the WSS. Numerical data for the luminal mesh discretization are provided in Table 3 and an illustration of the mesh construction is shown in Figure 14 (d). Luminal mesh parameters for the results presented hereafter are chosen after a mesh convergence study (see appendix B).

## 2.2 Intimal hyperplasia modelling

The multiscale compartmental model of IH presented in [12] describes the kinetic of vascular species in layers of a spatial domain called compartment. It considers cellular populations as vascular smooth muscle cells (vSMCs) — through their phenotypical state, contractile (cSMCs) and secretory (sSMCs) — endothelial cells (ECs), and non cellular population as young and old collagen fibers. The model contains biochemical equations for growth factors (GFs) dynamics, organized in seven families.

In this paper, we apply our modelling of IH development on an axisymmetric idealized artery. This section is a brief presentation of the model in this novel geometrical configuration.

Each compartment of arterial volume is labeled with upper index, as are all variables localized in this compartment. The kinetic differential equations of our model have the same structure: they express the rate of variation in time of a variable denoted by index “i” as  $X_i^j$  in the compartment “j”. This rate of variation is set by the

sum of the functional properties (FPs). Each variable is either a species count or a growth factor amount. The generic form of model equation is therefore

$$\frac{dX_i^j}{dt} = M_i^j + f_i^0 X_i^j - f_i^1 X_i^j + \text{cp}^j \text{ in } \Omega_i^j \quad (4)$$

where  $M_i^j$  is a source term,  $f_i^0$  and  $f_i^1$  are two FPs — *e.g.* proliferation and apoptosis —  $\text{cp}^j$  are the coupling terms with other variables, and  $\Omega_i^j$  is the spatial domain. For the  $j^{\text{th}}$  compartment, the set of differential equations of the model can be written in vectorial form as

$$\frac{d\mathbf{y}^j}{dt} = \mathbf{f}(\mathbf{y}^j, \mathbf{y}^j(t - \tau_C), \tau_w^j), \quad (5)$$

where  $\mathbf{y}^j$  is the vector of variables composed of species and GFs,  $t$  is the time,  $\mathbf{y}^j(t - \tau_C)$  is the vector of variables evaluated at time  $t - \tau_C$  with  $\tau_C$  the collagen ageing delay,  $\tau_w^j$  is the magnitude of WSS and  $\mathbf{f}$  the right-hand-side vector function. Equations (5) is solved numerically for each compartment over a timespan between  $t_0$  and  $t_f$  with an initial condition  $\mathbf{y}^j(t_0) = \mathbf{y}_0^j$  and a given history  $\mathbf{y}^j(t) = \mathbf{h}^j(t)$  for  $t_0 - \tau_C \leq t < t_0$ . The resolution of the system (5) is done with a Runge–Kutta solver based on [17]. For better comparison of tri-dimensional model results with the one-dimensional test-case [12], we retain identical constants of the models, initial condition and history. See Jansen et al. [12] for a detailed description of the model, including species functional properties (SFPs) integrated, constant parameters, initial and historical conditions and numerical time-marching algorithm.

As mentioned, we apply here the IH model to the case of an axisymmetric idealized artery, using a tridimensional formulation. Keeping the compartmental approach, we consider an arterial wall mesh composed of  $N_{\text{TG}}$  compartments, in which we apply the set of equations (5). Figure 1 (Right) shows an illustration of the arterial wall mesh and the compartmental configuration, in which there is an absence of coupling between neighbouring compartments. Thus, the spatial dependences are implicit in (a) longitudinal direction due to the coupling with the local hemodynamical WSS and (b) radial direction by the use of modelled intima

and media layers of a compartment. The assumption of decoupled neighbouring compartments results in the neglect of phenomena applying in the longitudinal direction, such as molecular diffusion of GFs or cellular migration, which tend to spread out matter and, generally, homogenize it in space. Unfortunately, as we neglect these phenomena, we may produce, from this compartmental modelling, significant variability of tissue dynamics between several neighbouring compartments. So-called “non-biophysical gradient of dynamics” may arise within the compartmental arterial wall mesh, especially if the hemodynamical WSS, a derived variable of a CFD computation, is coarsely solved numerically. Macroscopically, non-biophysical gradients may thus produce stiff morphological changes of the artery which, over hemodynamical generations, can lead to a divergence of the simulation due to under-resolution of the mesh deformation. This imposes a fine discretization in zones of biophysical gradients. A mesh convergence study, presented in Appendix B, has permitted to set adequate values of  $N_{\text{TC}}$  and CFD mesh parameters.

Moreover, one can model threshold phenomena with the piecewise-defined Macaulay function noted  $\langle \cdot \rangle$ , for migration and dedifferentiation on vSMCs [12]. This may produce the arising of non-biophysical gradients in some regions. To avoid this, we introduce a modified Macaulay function (MMF), noted  $\langle \cdot \rangle^*$ , which is smoother than  $\langle \cdot \rangle$ . The MMF is

$$\langle x - x_0 \rangle^* = \begin{cases} \frac{(x - (x_0 + l_M))^2}{4l_M}, & \text{if } x \in [x_0 - l_M, x_0 + l_M] \\ \langle x - x_0 \rangle, & \text{otherwise,} \end{cases} \quad (6)$$

with  $x_0$  a threshold value and  $l_M$  the half smoothing distance. In the present study, this MMF function replaces the Macaulay function in the SFPs, *i.e.* migration and dedifferentiation of vSMCs.

## 2.3 Coupling methods in a bidimensional domain

The coupling methods introduced in [12] are suitable for 2D axisymmetric configuration. The coupling between hemodynamics/biochemistry and biochemistry/SFPs is the same as in the monodimensional case, except that WSS stimuli are now distributed over the length of the artery. The WSS

stimulating each compartment is the magnitude  $\tau_w$  of the WSS vector from CFD (equation (3b)), interpolated using cubic spline at each endothelium face centre of compartments. This allows to consider non-conforming meshes between luminal and parietal meshes, *i.e.* non-coincidence of vertices of the two domain meshes at the endothelial surface.

A specific strategy is developed for the coupling between hemodynamics and arterial wall remodelling. From a separation of timescales of tissues growth and hemodynamics and as in other studies [1, 5, 6], we continue to assume loose coupling between arterial tissue dynamics and hemodynamics under the inward-hypertrophic remodelling hypotheses [12]. As in our previous study, remodelling of the whole luminal mesh domain occurs if either of the following conditions is reached on any compartment

$$\frac{V_{\text{all}}^j - V_w^j}{V_1^j} > 1 + \varepsilon, \quad (7a)$$

$$\frac{V_{\text{all}}^j - V_w^j}{V_1^j} < 1 - \varepsilon. \quad (7b)$$

$\varepsilon$  is a remodelling parameter indicating hemodynamics sensitivity to tissues growth.  $V_{\text{all}}^j$  is the  $j^{\text{th}}$  whole constant arterial volume, calculated as  $V_{\text{all}}^j = \Delta z^j \pi (R_{\text{ext}}^j)^2$  with  $\Delta z^j$  and  $R_{\text{ext}}^j$  respectively the length of the compartment and the external radius of the  $j^{\text{th}}$  compartment.  $V_w^j$  is the  $j^{\text{th}}$  time-dependent arterial wall volume defined from species dynamic evolution (see [12, eq. 12c] for definition).  $V_1^j$  is the  $j^{\text{th}}$  morphological-generation-dependent luminal volume calculated as  $V_1^j = \Delta z^j \pi (R_1^j)^2$  where  $R_1^j$  is the luminal radius of the  $j^{\text{th}}$  compartment associated with the current hemodynamical generation. As soon as a remodelling is detected from the conditions (7), all the luminal volumes  $V_1^j$  are updated in accordance with the new arterial morphology. Considering criterions (7), we compute for each compartment the ratio of the luminal volume at tissue growth timescale  $V_{\text{all}} - V_w$  over the luminal volume at hemodynamic timescale  $V_1$ . More precisely, (7a) corresponds to a tissue loss with an enlargement of the lumen, and (7b) corresponds to a tissue growth with luminal narrowing. Both criteria (7) are defined as terminal events, *i.e.* terminate the

time integration when an event occurs and modify the set of equations before a possible restart. The method of automatic detection of hemodynamical remodelling is a novelty compared to previous studies [1, 5, 6] which consider constant intervals between two consecutive remodellings.

In monodimensional domain, the update of the morphology of an artery is trivial as we consider a unique compartment. Considering higher dimension, after arterial wall discretization into compartments, we integrate  $N_{\text{TG}}$  times the system of equations (5). Related to the spatially-dependent dynamics of intimal hyperplasia, induced by WSS distributions and/or initial conditions, any compartment can reach criteria (7). The strategy to handle correctly the update between two successive arterial generations is explained in the following, for the first arterial generation.

From  $N_{\text{TG}}$  initial conditions and histories at  $t = t_0$ , the time-marching algorithm starts until the desired final time  $t = t_f$ . If compartments experiment one of the terminal remodelling criteria (7), one has to locate the minimum instant from all compartments. This instant is the next restart time for the new time integration of (5) for all compartments of the parietal mesh, noted  $t_{\text{restart}}$ , and it is defined as

$$t_{\text{restart}} = \min_{\text{vj}}(t_f^j), \quad (8)$$

with  $t_f^j$  the final time of the  $j^{\text{th}}$  compartment. Once the restart time is known, we evaluate all the luminal radius of compartments along the artery at time  $t = t_{\text{restart}}$  to calculate the arterial morphology of the next morphological generation :  $R_{k+1}(z) = R^j(t_{\text{restart}})$ . Using  $R_{k+1}$ , we apply a mesh motion on the luminal mesh to generate the next one.

Considering axisymmetric luminal morphological changes, we can manage mesh motion with a simple algebraic expression assuming only radial mesh vertices displacement while retaining good mesh properties over morphological changes, such as mesh non-orthogonality and skewness. An illustration of a CFD mesh motion is given in Figure 2 where discreet compartmental radius  $R^j$  and the morphological changes  $R_1(z) = R(t_{\text{restart}})$  are represented. A cubic spline interpolation is used to evaluate luminal radius from the centre of compartments to the vertices of the boundary surface

$\Gamma_1^e$ , noted  $R_1^{l,N_r}$  (see Figure 2). Considering the mesh motion for the generation  $k+1$ , the algebraic relation for radial coordinate of the mesh vertices, noted  $r_{k+1}^{l,n}$ , read

$$r_{k+1}^{l,n} = r_0^{l,n} E_{k+1}^l \quad (9)$$

with  $l$  and  $n$  respectively the longitudinal and the radial increment,  $r_0^{l,n}$  radial position of initial mesh generation and  $E_{k+1}^l = R_{k+1}^{l,N_r}/R_0$  the radial deformation from initial configuration.

Once the mesh is updated thanks to equation (9), a next cycle starts as: computing a new CFD simulation according to the novel arterial morphology and luminal mesh, then updating the set of equations (5) based on a new WSS distribution, and finally, restarting the time integration of IH model until reaching  $t_f$  or detecting a new remodelling criteria and starting again the whole procedure.

Another situation is the return to an equilibrium state of the entire wall during the resorption of the pathology, or when a new equilibrium is reached as in our test-case [12]. We add, to the terminal remodelling criteria, a non-terminal stopping criterion and suppose that the arterial wall return to equilibrium if all compartments check

$$\left\| \left[ \frac{d\mathbf{y}^\dagger}{dt^\dagger} \right]^j \right\| < \epsilon, \quad (10)$$

where  $\epsilon$  is the equilibrium sensitivity parameter,  $\|\cdot\|$  the  $L_2$  norm and  $\left[ \frac{d\mathbf{y}^\dagger}{dt^\dagger} \right]^j$  the dimensionless time derivative  $\mathbf{y}$  of the  $j^{\text{th}}$  compartment (see [12] for the definitions of dimensionless variables).

## 2.4 Disendothelization models

Considering the same approach as in our validation test-case [12], we investigate the response of the artery to mechanically-induced local damages. A localized damage of the endothelial cell (EC) layer disturbs the homeostatic equilibrium of our model and it initiates a tissue growth response, already described in [12].

These damages are imposed as initial conditions for the equations governing the evolution of ECs. They are limited to a defined region in the longitudinal direction in  $z \in [z_l, z_u]$  with  $z_l$  and  $z_u$  respectively the lower and upper longitudinal limits of the damages.



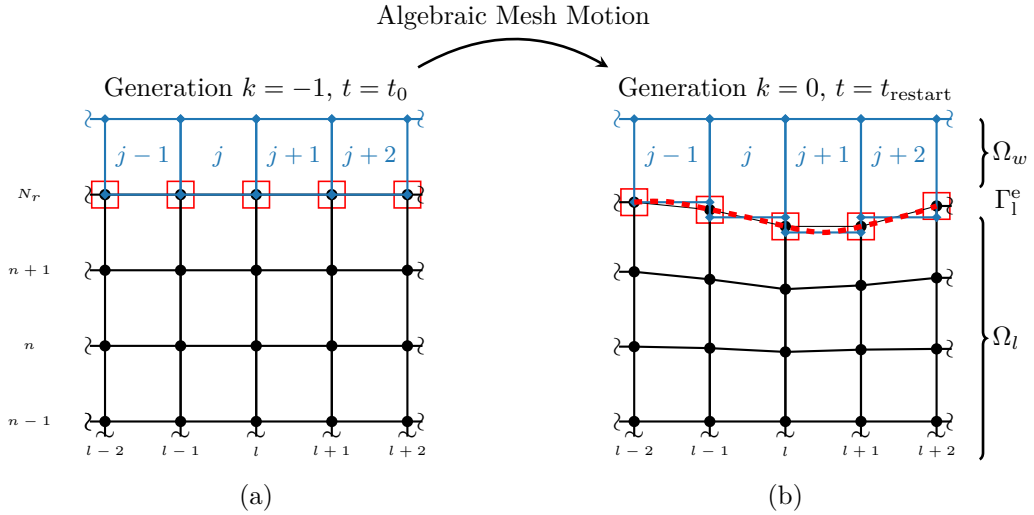


**Fig. 2:** Algebraic mesh motion strategy between two luminal meshes with (a) a first straight initial generation  $k = -1$  and (b) a second deformed generation  $k = 0$  at restart time  $t_{\text{restart}}$ . Part of luminal mesh (solid line with circular vertices) and parietal mesh (solid line with diamond vertices and compartment labeled with index  $j$ ) are illustrated on both sides of the endothelium surface  $\Gamma_1^e$  at the interface between luminal domain  $\Omega_l$  and parietal domain  $\Omega_w$ .  $l$  and  $n$  are respectively increment in the longitudinal and radial direction labeling vertices in meshes. Cubic spline interpolation (dashed line in (b)) of luminal radius of compartments at  $t = t_{\text{restart}}$  permit to evaluate new luminal vertices at  $\Gamma_1^e$  noted  $R_1^{l, N_r}$  (surrounded with square). Using the algebraic mesh motion relation (9), all the vertices of the luminal mesh are moved as seen in (b).

497 Firstly, we consider, using hyperbolic tangent  
498 functions, a so-called bump damage (BD) of the  
499 form

$$E_0^\dagger(z) = 1 + \frac{1 - d_0}{2} \left[ \tanh\left(-\frac{z - z_1^{\text{BD}}}{\delta_z}\right) + \tanh\left(\frac{z - z_u^{\text{BD}}}{\delta_z}\right) \right], \quad (11a)$$

500 with  $E^\dagger$  the ECs count  $E$  divided by its maxi-  
501 mal value  $E_{\text{max}}$ ,  $\delta_z$  parameter to adjust the length  
502 of transition zone between healthy and damaged  
503 zone,  $d_0$  initial damage parameter and  $z_{u,1}^{\text{BD}}$  limits  
504 of the damaged zone.

505 Another gaussian damage (GD) is applied,  
506 using gaussian function, as

$$E_0^\dagger(z) = 1 - d_0 \exp\left(-\frac{(z - z_G)^2}{2\sigma_G^2}\right), \quad (12)$$

507 with  $z_G$  centre of the damaged zone and  $\sigma_G$   
508 the damage length control parameter. Lower and  
509 upper limits of GD are respectively defined as

510  $z_1^{\text{GD}} = x_G - 1.18\sigma_G$  and  $z_u^{\text{GD}} = x_G + 1.18\sigma_G$  so  
511 that for both damages we get  $E_0^\dagger(z_{u,1}) = 0.5$ .

512 Figure 3 presents the two analytical dam-  
513 age functions chosen in equations (11) and (12).  
514 In a region of equivalent length, the considered  
515 damages model the following two types of dis-  
516 endothelization as

- a focal damage, where endothelium is strongly injured on the major part of the damage zone and where transition between healthy and damaged zone is stiff;
- a diffuse damage, where the disendothelization is severe on a small zone with smooth transition between healthy and damaged zone.

524 The comparison of two different initial damages  
525 aims to quantify the influence of initial conditions  
526 on the lesion developments predicted by our model  
527 of IH in an axisymmetric artery at  $Re_0 = 300$ .

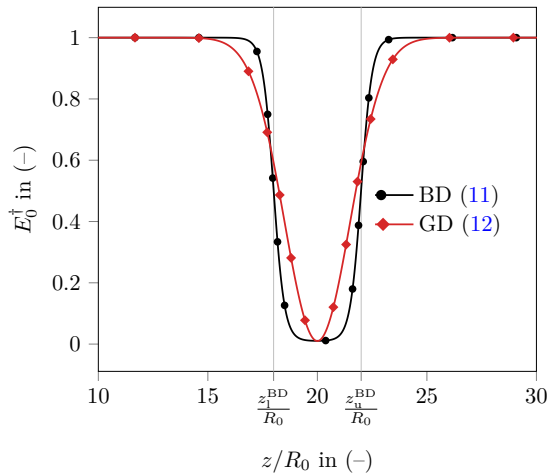


**Fig. 3:** Gaussian (diamond symbols) and bump (circle symbols) damages applied to the endothelium at initial time.  $x$ -axis is the dimensionless longitudinal position  $z/R_0$  and  $y$ -axis is the initial value of  $E_0^\dagger = E_0/E_{\max}$  the rescaled endothelial cells population with  $E$  the ECs count and  $E_{\max}$  the maximal value.

### 3 Results and Discussions

First, we present in section 3.1 the macroscopic spatio-temporal evolution of lesions with: in section 3.1.1, an analysis of remodelling dynamics via the detection of criteria (7); in section 3.1.2, a discussion on the dynamics of the luminal radius in both damages; in section 3.1.3, a comparison of mono- and bi-dimensional results in terms of luminal radius and WSS to discuss the main differences between cases; in section 3.1.4, an evaluation of the mesh motion procedure as well as CFDs resolutions.

Finally, we consider microscopic scales in section 3.2. The macroscopic dynamics is induced by the species dynamics, that we present in the following sections: 3.2.1, presenting the ECs regenerations; 3.2.2, discussing the various functional properties of vSMCs; 3.2.3, discussing the dynamics of sSMCs populations within intima and media layers and 3.2.4, presenting the composition of intimal layer during the development of the lesions.

#### 3.1 Macroscopic lesion evolution

##### 3.1.1 Detection of remodelling criteria

Firstly, we present the spatio-temporal evolution of the detection of criteria (7) inducing hemodynamical remodelling. As this type of automatic remodeling has never been implemented to our knowledge, we present in detail the detections of remodeling events which have a non-trivial behavior. Figure 4 shows the instants where hemodynamical remodellings are performed, for gaussian and bump damages. For each data point in this figure, a terminal event from criteria (7) has been located. Depending on the remodelling times, we report the associated dimensionless longitudinal position within the artery of the compartment which experimented this event, noted  $z_c/R_0$ , along with its dimensionless radius  $R_c/R_0$ . This figure gives an overview of the dynamics of lesions through the evolutions of events detection. Reading this graph helps to locate longitudinal zones and time intervals of interest in the lesion developments.

Between 0 and 10 days, both damages exhibit the same evolution of the detection of events spatially and temporally. The hotspots of tissues growth are localized at the centre of the damaged zones ( $z/R_0 \sim 20$ ) and the compartmental radius  $R_c$  decrease is the same. During the first ten days, hotspots of tissues growth move slightly downstream of the initial maximal damaged point at  $z/R_0 = 20$ .

From day 10, GD and BD cases stop having the same behaviour. The GD compartmental radius  $R_c^{\text{GD}}$  decrease slows down and reaches its minimal radius ( $R_c^{\text{GD}} = 0.91R_0$ ) on day 19 and at longitudinal position  $z_c^{\text{GD}} = 20.4R_0$ . However, the BD compartmental radius  $R_c^{\text{BD}}$  still decreases until reaching a first minimal radius ( $R_c^{\text{BD}} = 0.89R_0$ ) on day 17.6 at longitudinal position  $z_c^{\text{BD}} = 20.8R_0$ . During these two luminal radius decrease phases, the detected events are all of the narrowing type (7b).

The two dynamics of criteria detection diverge around day 20. We begin with the discussion of GD lesion evolution, before that of the BD lesion in the next paragraph.

For the GD case, there is a breakpoint in the lesion dynamics at day 21.5 materialized by the detection of a first enlargement criterion (7a) at longitudinal position  $z_c^{\text{GD}} = 20.1R_0$ . This new type of event detected produces a gap in  $z_c/R_0$

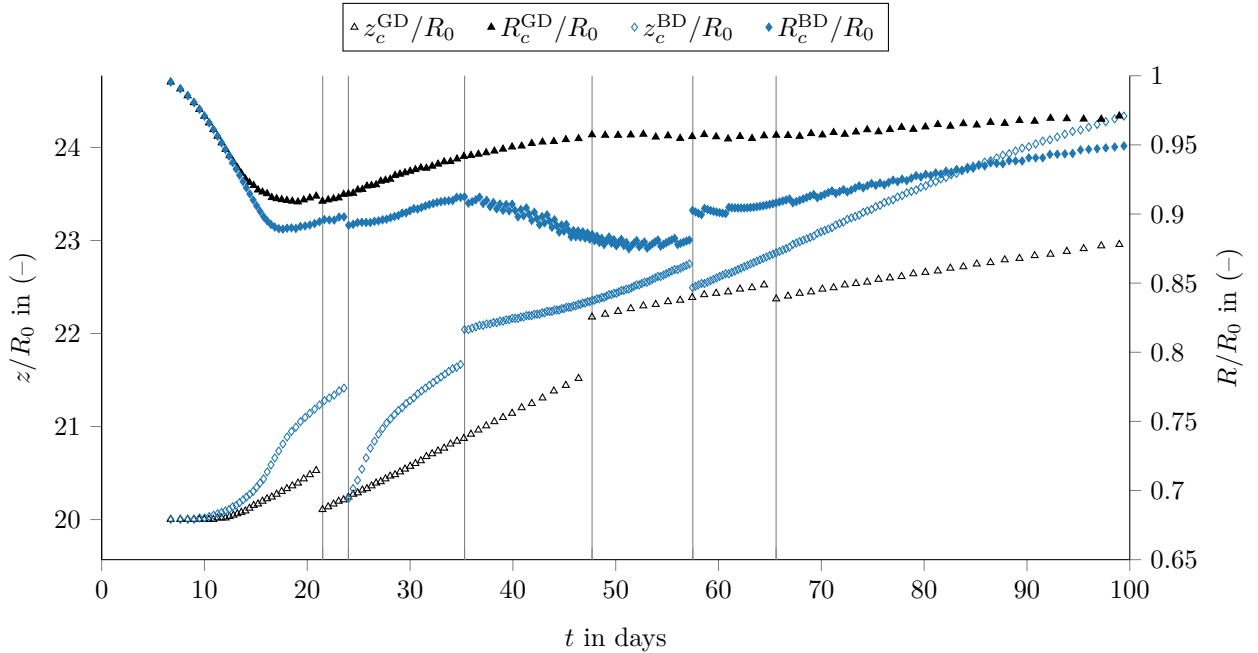


**Fig. 4:** Instants of narrowing and enlargement events detected during the gaussian (GD) and bump (BD) damages. Left  $y$ -axis: Longitudinal position normalized by the initial radius  $z/R_0$ . Right  $y$ -axis: Luminal radius normalized by  $R/R_0$  at the instant of detection. Vertical lines highlight the switch from one type of event detected to another.

601 evolution (shown with vertical lines in Figure 4). 625  
 602 This reflects the fact that, after approximately 626  
 603 20 days in the zone initially damaged, there is 627  
 604 a stronger resorption of the lesion in the initial 628  
 605 damaged zone than a tissue growth occurring 629  
 606 downstream of  $z/R_0 = 20$  (see Figure 5). This 630  
 607 lesion resorption has been presented in our previ- 631  
 608 ous work [12] and will be discussed in section 3.2 632  
 609 at the cellular scale. For  $t \in [21.5, 46.4]$  days, 633  
 610 only enlargement criteria are detected in GD. At 634  
 611  $t = 47.7$  days, another gap in  $z_c^{\text{GD}}/R_0$  evolution 635  
 612 is seen. It points out the detection of narrow- 636  
 613 ing events (7b) localized downstream the initial 637  
 614 damaged zone ( $z_c^{\text{GD}} = 22.2R_0$ ). Finally, a last 638  
 615 switch from narrowing to enlargement criterion is 639  
 616 seen on day 65.6. Until  $t = 100$  days, the GD 640  
 617 compartmental radius  $R_c^{\text{GD}}$  grows slowly. 641

618 For the BD lesion, the first switch from narrow- 642  
 619 ing to enlargement events is seen after that of GD 643  
 620 on day 24 at longitudinal position  $z_c^{\text{BD}} = 20.2R_0$ . 644  
 621 Between this instant and until day 35.3, only 645  
 622 enlargement events are detected and the luminal 646  
 623 radius  $R_c^{\text{BD}}$  increases. From day 35.3 to day 57.2, 647  
 624 the last switch of type of event, the lesion gets

into another growing phase downstream the dam-  
 aged zone. The BD lesion reaches the minimum  
 compartmental luminal radius at event instants  
 ( $R_c = 0.87R_0$ ) at  $t = 51.3$  days at the longitudi-  
 nal position  $z_c^{\text{BD}}/R_0 \sim 22.5$ . Finally from day 57.5  
 until  $t = 100$  days, events detected are all of the  
 enlargement type (7a) and  $R_c^{\text{BD}}$  grows slowly as  
 for GD lesion.

In summary, the number of events detected  
 after 100 simulated days for GD and BD lesion are  
 respectively 110 and 249 for as many CFDs carried  
 out. On day 100, the BD case causes about twice  
 as many remodelling as the GD case, whereas at  
 $t \sim 40$  days the number of criteria detected for  
 the GD and BD cases are respectively 63 and  
 86. This important difference, in terms of number  
 of remodelling between the two cases, is due  
 to the important phase of tissue growth down-  
 stream of the initial damage in the BD lesion (see  
 Figure 5). Thus, the lesion dynamics downstream  
 of the initial injury, induced by the dynamics of  
 the underlying vascular species, in the BD case  
 is exacerbated compared to the GD case. We will

discuss the phases of narrowing observed downstream of the initial damages seen in Figure 4, for the BD between  $z_c^{\text{BD}}/R_0 \in [22, 22.7]$  and for the GD between  $z_c^{\text{EG}}/R_0 \in [22.2, 22.5]$ , in section 3.2 by presenting the dynamics of vascular species in these zones.

The minimum time interval between two successive hemodynamical generations is for the GD and BD cases respectively of 0.38 days ( $\sim 3.2892 \times 10^4$  seconds) and 0.227 days ( $\sim 1.9613 \times 10^4$  seconds). This result supports our hypothesis of timescale separation between tissue growth and hemodynamics, which assumes a succession of quasi-static states over the course of pathological development.

### 3.1.2 Evolution of the luminal radius

We discuss the spatio-temporal evolutions of the luminal radius of arteries in the pseudo-color plots in Figures 5 (a,b). Throughout this article, plots of this type are obtained from Gouraud (bi-linear) interpolation of the data from the simulations of the model on the compartmental mesh of the arterial wall. Figures 5 (a,b) allow the overall visualization of the onset of lesions and displacements downstream of the damaged zones. In addition, snapshot of luminal morphologies over several instants permit a quantitative comparison between the two types of initial damages in Figures 5 (c,d).

Regarding Figures 5 (a) and (b), and as already described with event detections in section 3.1.1, we observe between 0 and 20 the lesion onset in the damaged zones for both cases. After 20 days, the lesions develop downstream from the initial injury, strongly for the BD lesion that reached the longitudinal position  $z \sim 24.1R_0$  at day 100, and to a lesser extent for the GD lesion reaching  $z \sim 22.9R_0$  at day 100. In both cases, this displacement is explained by the WSS distribution downstream the incipient lesion between 0 and 20 days (see Figures 8 and 9) which induces a prone zone to hyperplasia (see Figure 12).

We compare the maximum predicted stenoses in the two simulations. In GD case, the maximal lesion ( $R_1 = 3.56$  mm) is observed at  $t = 20.9$  days at  $z \sim 20.3R_0$ . From there, the lesion decreases as it continuously moves downstream. On the contrary, the maximal lesion in the BD case ( $R_1 = 3.439$  mm) is observed at  $t = 54.1$  days at  $z \sim$

$22.5R_0$ . Furthermore, we also observe in BD a growth of the same intensity ( $R_1(t = 20\text{d}, z \sim 20.5R_0) = 3.453$  mm) at day 20 around the centre of the artery (see Figure 5 (d)). This highlights the main difference between the two models of damage: the BD lesion meets another important tissue growth phase during its downstream movement. Thus, the downstream zones of stenosis may be more prone to tissue growth induced by wall shear stress values, than the initially damaged zone where tissue growth is provoked by a disturbance of the homeostatic equilibrium.

The difference of spatio-temporal evolution of  $R_1(t, z)$  is mainly due to the morphological differences of the lesions at short time which drive the longitudinal variation of WSS (see Figure 8). In GD case, the stenosis is smoother than in the BD case (see Figures 5 (c) and (d) at  $t = 30, 40, 50$  days). These morphological differences induce lower WSS downstream of the lesion for the BD case as shown in Figure 8 from  $t > 15$  days. Our model associated with the BD case therefore predicts an important growth phase not induced by the injury but by the distribution of WSS, which goes in the direction of the macroscopic hypotheses on the importance of pathology-promoting zones with “disturbed flow” [15, 20]. This result is built only from biochemical and cellular hypotheses proposed in [12]. We describe in section 3.2 the dynamics of vascular species inducing tissue growth in zones of low WSS.

As soon as the lesion begins to move downstream, this initiates self-maintenance of this displacement. Indeed, downstream of a developing stenosis, a new pathology-promoting zone will appear because of low WSS values. We refer the reader to Figure 9 showing the evolution of the minimum of WSS over the time and the longitudinal position. These distributions of WSS explain the continuous downstream movement of the lesion which is indicated by arrows in Figure 5 (a) and (b).

### 3.1.3 Comparison between 1D and 2D geometries

At the centre of the two damaged zones ( $z/R_0 = 20$ ), we compare in Figure 6 axisymmetric and monodimensional results through the temporal evolution of luminal radius and WSS.

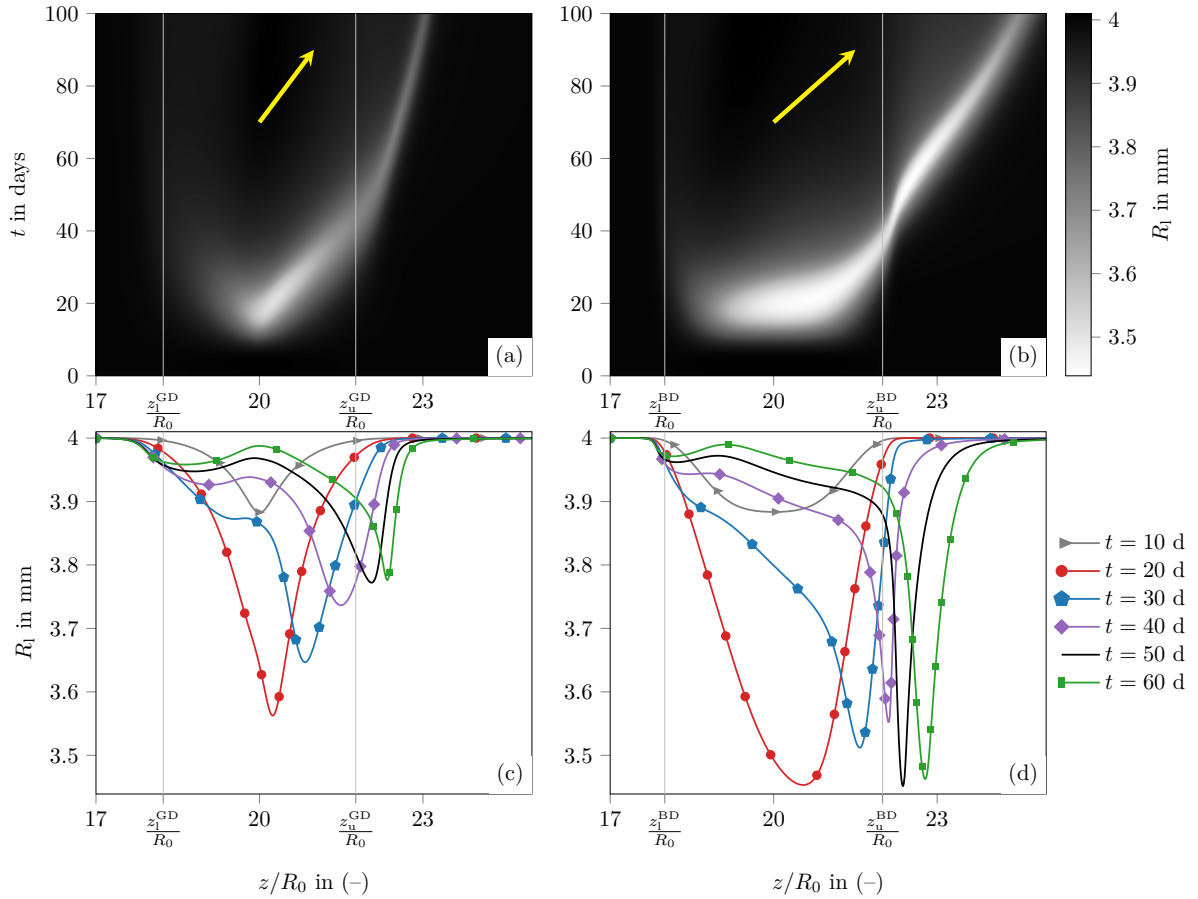


**Fig. 5:** Spatio-temporal evolution of the luminal radius  $R_1(t, z)$  for gaussian (a) and bump (b) damages.  $x$ -axis is the dimensionless longitudinal position  $z/R_0$ . For (a) and (b),  $y$ -axis is time in day. Arrows show the displacement of lesions downstream of the initial damaged zones. Snapshots of  $R_1(t, z)$  at 10, 20, 30, 40, 50 and 60 days are drawn in GD (c) and BD (d) cases.

745 Figure 6 (a) presents the evolution of WSS 761  
 746 between 0 and 100 days in 1D and axisymmetric 762  
 747 cases. We observe the same global dynamics 763  
 748 of WSS dictated by the phases of lumen narrow- 764  
 749 ing and enlargement, respectively inducing the 765  
 750 phase of increase and decrease of WSS. However, 766  
 751 these phases have neither the same timescales nor 767  
 752 the same amplitudes. We explain these differences 768  
 753 because in the 1D case, we assume an infinitely 769  
 754 pathological artery without taking into account 770  
 755 the converging and diverging zones of the blood 771  
 756 flow upstream and downstream of the stenosis 772  
 757 resulting from the tissue growth. These zones of 773  
 758 flow acceleration and deceleration, on either side 774  
 759 of the lesion, produce this WSS-observed increase 775  
 760 in the axisymmetric configuration. 776

We also observe a deviation of the duration of  
 the growth phase of WSS between mono- and bidi-  
 dimensional configuration, *i.e.* in GD  $\tau = 18$  days,  
 in BD  $\tau = 20.7$  days and in 1D case  $\tau = 22.6$  days.  
 These timescale deviations from 1D test-case, are  
 due to the differences in the intensities of the WSS.  
 Indeed, when the arterial wall is subjected to a  
 WSS higher than the physiological-initial value,  
 our model promotes lesion resorption to the detri-  
 ment of tissue growth due to the bioavailability of  
 growth factors. The higher the WSS, the greater  
 the biochemical state of protection against tissue  
 growth and the shorter the phase of tissue growth,  
*e.g.* with the minimum phase of growth ( $\tau = 18$   
 days) for the maximum values of WSS. Thus, this  
 contraction of the duration of tissue growth is

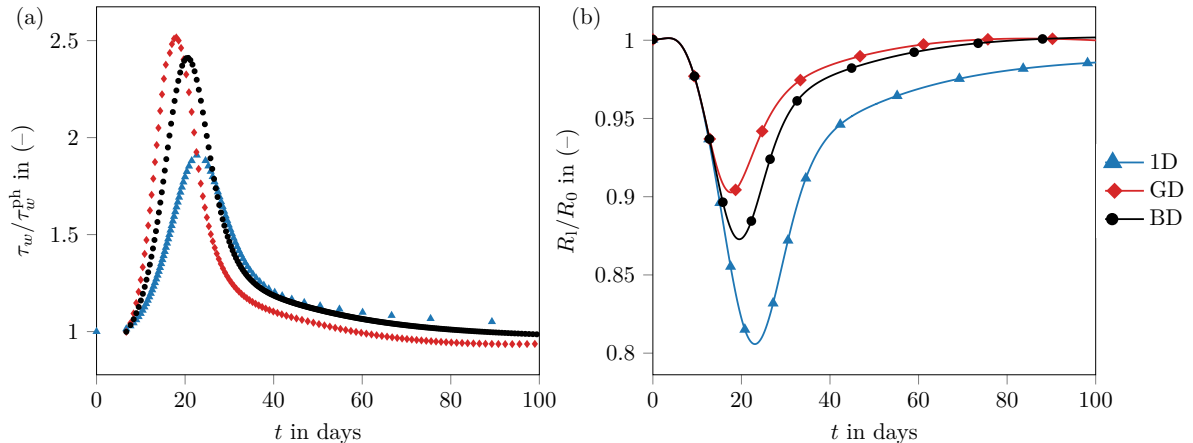


**Fig. 6:** Comparison between 1D case-test [12] (triangle symbols), GD (diamond symbols) and BD (circle symbols) cases at the compartment localized at  $z/R_0 = 20$  between 0 and 100 days. (a) WSS normalized by the physiological value  $\tau_w/\tau_w^{\text{ph}}$  along the arterial generations. (b) Normalized luminal radius  $R_l/R_0$  as function of time.

777 maximum in the GD case, compared to the other 806  
778 cases, because the WSSs in this case are higher. 807

779 Figure 6 (b) compares the evolution of the 808  
780 luminal radius for the three cases. As for the 809  
781 dynamics of the WSS,  $R_l/R_0$  follows the same 810  
782 phasic evolution with tissue growth followed by 811  
783 tissue loss. In bidimensional cases, the lesions 812  
784 are less severe than the 1D case, although they 813  
785 are induced by the same initial disendothelization 814  
786 ( $E^\dagger(t_0, z = 20R_0) = 1 - d_0$ ). It is mainly due 815  
787 to the higher WSS discussed below. It emerges 816  
788 from this comparison that the hypothesis of 817  
789 monodimensional configuration, *i.e.* an infinitely 818  
790 long damage, posed to test our model in a simple 819  
791 one-dimensional configuration, has a strong 820  
792 importance on lesion development at  $z/R_0 = 20$  821  
793 especially at short time. 822

### 3.1.4 Arterial generations: CFD 823 resolutions and wall shear stress 824 stimuli 825

797 In Figure 7 (a), by plotting the maximum of the 826  
798 faces non-orthogonality parameter  $\theta_{\text{face}}^{\text{max}}$  returned 827  
799 by the `checkMesh` utility of `OpenFOAM`, we assess 828  
800 the quality of CFD meshes in GD and BD cases 829  
801 of all the arterial generations created from the 830  
802 moving mesh strategy introduced in section 2.3. 831  
803 As supposed, the variations of  $\theta_{\text{face}}^{\text{max}}$  in the GD 832  
804 case (maximum of  $12.74^\circ$  at the  $85^{\text{th}}$  genera- 833  
805 tion) are limited compared to the BD case 834

806 which predicts stiffer luminal morphologies (see 807  
808 Figure 5 (d)). The  $\theta_{\text{face}}^{\text{max}}$  parameter in BD increase 809  
810 then decreases as tissue growth loses intensity (see 811  
812 Figure 5). 813

814 To illustrate a mesh obtained by the algebraic 815  
816 mesh motion algorithm in the period where 817  
818  $\theta_{\text{face}}^{\text{max}} > 30^\circ$ , we propose a `ParaView` visualization 819  
820 in Figure 7 (c) of  $84^{\text{th}}$  arterial generation at 821  
822  $t = 39.9$  days. The mesh, visible in black lines, 823  
824 is coloured by the non-orthogonality of cells field 825  
826  $\theta_{\text{cell}}^{\text{max}}$ . The maximum non-orthogonality is local- 827  
828 ized downstream of the stenosis and near the wall, 829  
830 in the zone where the variations in the lumi- 831  
832 nal radius are stiffer. According to the maximum 833  
834 value of  $\theta_{\text{face}}^{\text{max}}$  in Figure 7 (a) and the general 835  
836 appearance of a stiff arterial morphology mesh in 837  
838 Figure 7 (c), we can validate the proposed algebraic 839  
840 mesh motion strategy in the two types of 841  
842 damage considered here. 843

844 We now study the convergence of hemody- 845  
846 namics simulations during the pathological develop- 847  
848 ment in the BD case. In Figure 7 (b), we plot, as a 849  
850 function of arterial generations, the final pressure 851  
852 and velocity normalized residuals of the SIMPLE 853  
854 algorithm. The values of the residues reported are 855  
856 those of the final state of the numerical resolution 857  
858 at each arterial generation and not a continuous 859  
860 variation of residuals. 861

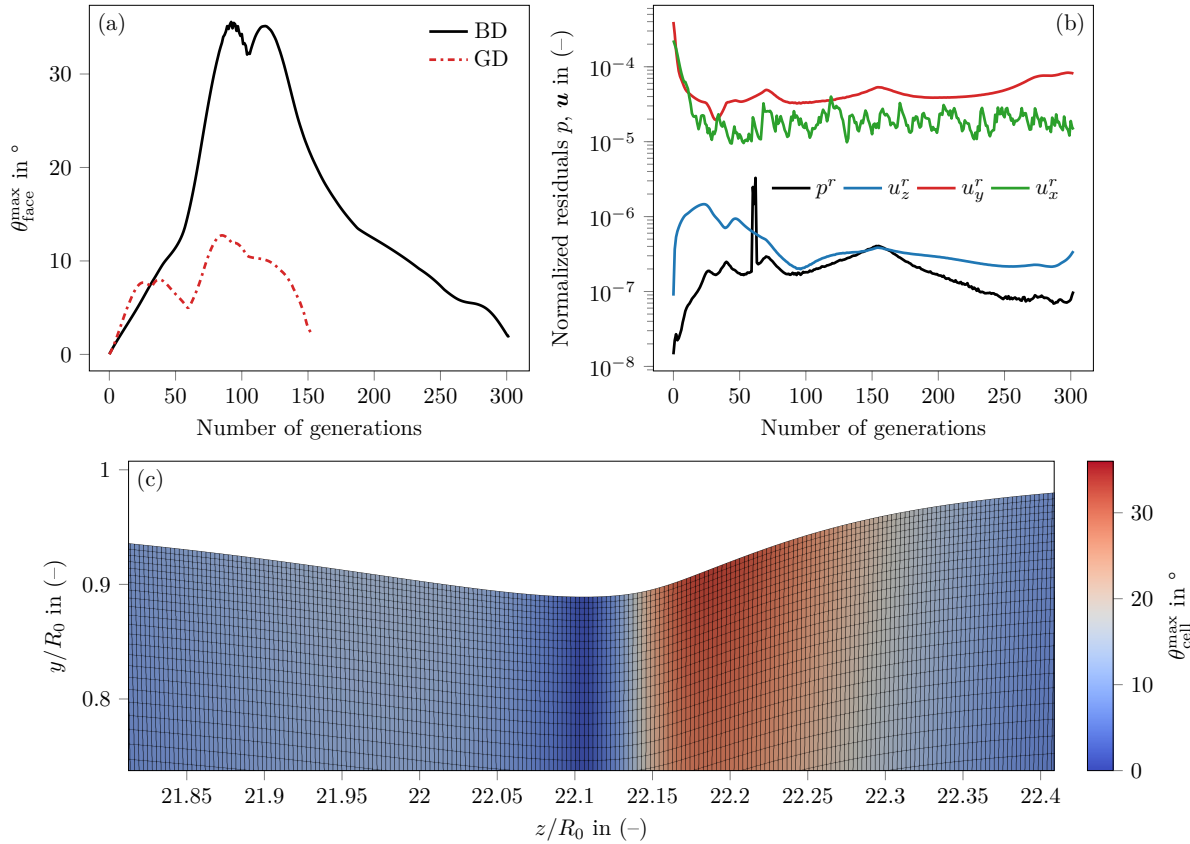


**Fig. 7:** (a) Maximum face non-orthogonality parameter  $\theta_{\text{face}}^{\text{max}}$  as a function of the generated luminal meshes (number of arterial generations calculated) in gaussian damage (dashed lines) and bump damage (solid lines). (b) Normalized residuals of pressure and velocity at the last SIMPLE iteration as a function of arterial generations in BD case. (c) ParaView mesh visualization of the 84<sup>th</sup> arterial generation at  $t = 39.9$  days in the stenosis zone of the BD case. In pseudo-colors, the cell non-orthogonality parameter field  $\theta_{\text{cell}}^{\text{max}}$  is presented.

835 This plot shows that all the hemodynamics sim- 851  
 836 ulations are sufficiently converged. The maximum 852  
 837 normalized residuals for all generations are respec- 853  
 838 tively  $p_{\text{max}}^r = 3.29 \times 10^{-6}$ ,  $u_{z\text{max}}^r = 1.46 \times 10^{-6}$ , 854  
 839  $u_{y\text{max}}^r = 3.96 \times 10^{-4}$ ,  $u_{x\text{max}}^r = 2.25 \times 10^{-4}$ . 855

840 Finally, to conclude on the macroscopic vari- 856  
 841 ables, the spatio-temporal variations of WSS are 857  
 842 presented. We show in Figure 8 the spatial varia- 858  
 843 tions of WSS over several arterial generations in 859  
 844 GD and BD cases. Since the two damage models 860  
 845 present different lesion dynamics, there is no arte- 861  
 846 rial generation having in common the same instant 862  
 847 of remodelling in GD and BD. However, wishing 863  
 848 to compare the WSS at equivalent times in both 864  
 849 cases, we present in Figure 8 the hemodynamic 865  
 850 generations having similar remodelling instants. 866

851 These moments of generations — denoted by 914  
 852  $t_{k_{\text{GD}}, k_{\text{BD}}}$  with  $k_{\text{GD}}$  and  $k_{\text{BD}}$  respectively the gener- 915  
 853 erational indexes of GD and BD cases — are 916  
 854 respectively  $t_{-1,-1} = 0$  d,  $t_{6,6} = 10.0$  d,  $t_{17,18} =$  917  
 855  $14.8$  d,  $t_{28,32} = 20.3$  d,  $t_{36,41} = 24.9$  d,  $t_{48,55} =$  918  
 856  $30.0$  d,  $t_{57,69} = 35.2$  d et  $t_{63,83} = 39.9$  d. 919

857 As already compared at  $z/R_0 = 20$  (see Figure 920  
 858 6), at short timescale in the strongly damaged 921  
 859 zone, the WSS of the GD case is higher than that 922  
 860 of the BD case. Quickly, from  $t = 20$  days, the 923  
 861 maximum of WSS in both cases move downstream 924  
 862 of the initial damaged zone. In the meantime, a 925  
 863 zone of low WSS ( $\tau_w/\tau_w^{\text{ph}} < 1$ ) appears down- 926  
 864 stream of the maximums. The form of the initial 927  
 865 damage over time determines the forms taken by 928  
 866 the lesion during its development and the resulting

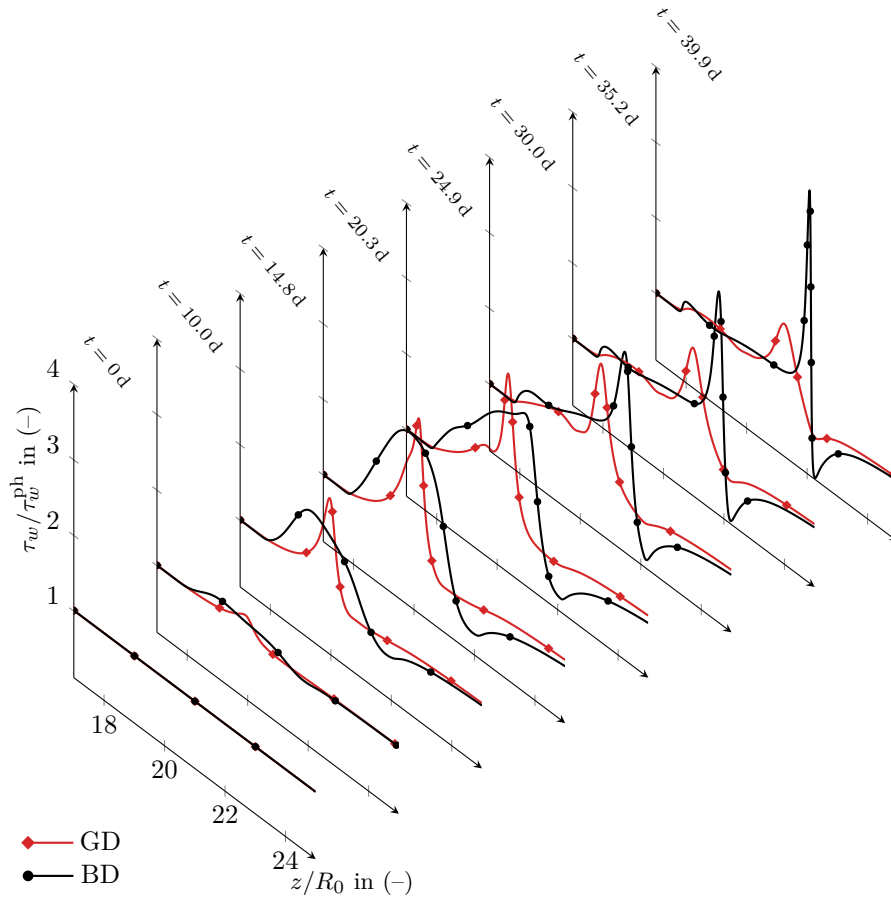


**Fig. 8:** Spatial variations of the normalized magnitude of the wall shear stress  $\tau_w/\tau_w^{\text{ph}}$  for several arterial generations for gaussian (diamond symbols) and bump damage (circle symbols).

867 WSS shapes. In the GD model, the lesion forms a  
 868 rather intense peak up to  $t = 20$  days (see Figure  
 869 5) and we find this form in the spatial variation  
 870 of the WSS for  $t = 10, 14.8, 20$  days with a lower  
 871 wall shear stress zone downstream.

872 On the other hand, after 20 days, the locations  
 873 of the lowest WSS exerted downstream of  
 874 the initial damage are correlated, with a delay  
 875 effect, with the zones of tissue growth responsible  
 876 for the macroscopic lesion displacement (see  
 877 Figure 5). After 20 days, the longitudinal distribution  
 878 of WSS drives the lesion dynamics according to  
 879 Figure 5 and 8. The other important result to  
 880 be drawn from Figure 8 is that the displacement  
 881 of the maximum of WSS, as well as its value, is  
 882 exacerbated in the BD model compared to the GD  
 883 model. This remark also applies to the minima of  
 884 WSS which are lower in bump damage.

885 In order to quantify the displacement and the  
 886 values of the extremum of WSS during the two  
 887 models of damage, we follow respectively the tra-  
 888 jectories of the maximum and the minimum of  
 889 WSS at each arterial generation in the gaussian  
 890 and bump damages, noted  $\tau_w^{\text{max}}(t, z), \tau_w^{\text{min}}(t, z)$ ,  
 891 in Figures 9 (a) and (b). In BD, the maximum  
 892 of  $\tau_w^{\text{max}}(t, z)$  appears during the phase of down-  
 893 stream displacement of the lesion (at  $t = 47$  days  
 894 at  $z/R_0 \sim 22.3$ ), while it is observed at  $t = 23$   
 895 days at  $z/R_0 \sim 20.3$  in GD model. The minimum  
 896 of  $\tau_w^{\text{min}}(t, z)$  occurs in time and space in BD and  
 897 GD respectively at  $t \sim 39$  days and at  $z/R_0 = 22.2$   
 898 and at  $t = 52.7$  days and at  $z/R_0 = 22.5$ . The  
 899 bump damage induce smaller WSS values, *e.g.*  
 900  $\tau_w^{\text{min}}/\tau_w^{\text{ph}} < 0.2$ , than the gaussian damage model.  
 901 Moreover, according to this figure, no recirculation  
 902 zone, detectable when  $\tau_w^{\text{min}} = 0$ , is generated



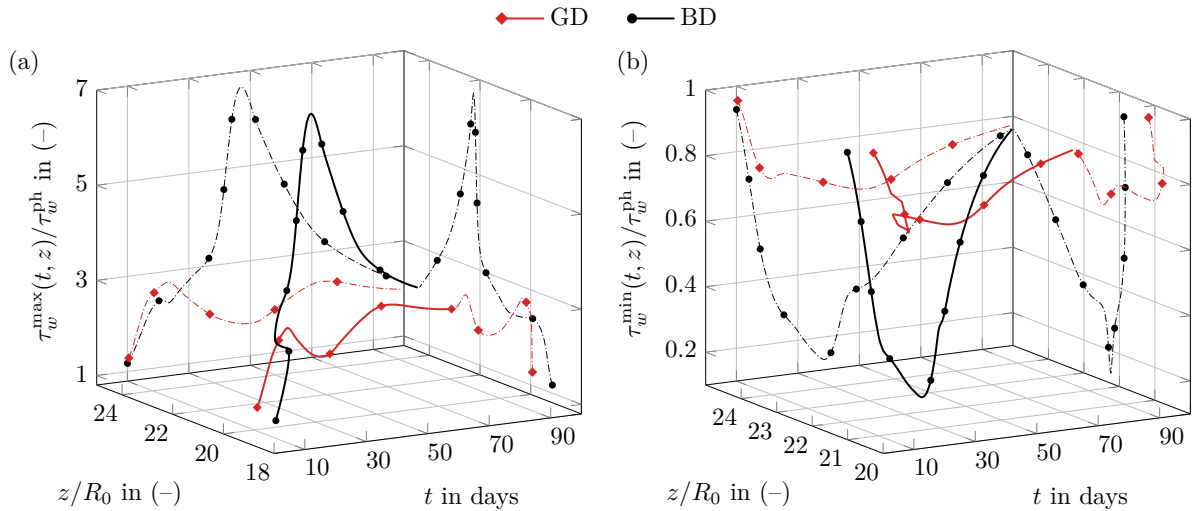


**Fig. 9:** Trajectories (solid lines) of the maximum (a) and minimum (b) normalized wall shear stress  $\tau_w/\tau_w^{\text{ph}}$  during lesion development in the gaussian (diamond symbols) and the bump damage (circle symbols). For a clear visualization of these three-dimensional trajectories, projections are proposed on the planes  $(z/R_0, \tau_w/\tau_w^{\text{ph}})$  and  $(t, \tau_w/\tau_w^{\text{ph}})$  in dotted lines.

during the development of the lesion in both models of damage. To quantify the delay between low levels of WSS and promotion of tissue growth predicted by our model, we compare the instant and location of the smallest WSS value in BD ( $t \sim 39$  days at  $z/R_0 = 22.2$ ) with the instant and location of the strongest stenosis ( $t = 54.1$  days at  $z = 22.5R_0$ ). We notice a time lag of about 15 days between these two events while spatially these two extremes coincide.

## 3.2 Spatio-temporal dynamics of tissues growth

### 3.2.1 Endothelium regeneration

We present the ECs response to the two models of damage. Figures 10 (a) and (b) show the spatio-temporal evolution of the ECs population in term of  $E^\dagger(t, z)$ , the rescaled EC count by its maximal value at each compartment as  $E^\dagger(t, z) = E(t, z)/E_{\text{max}}(z)$ . ECs follow a logistic dynamics not coupled with other variables of the model, thus Figure 10 presents different logistic dynamics for each compartment which differ only from the initial condition applied. Figure 10 (c) shows the dynamics of ECs regeneration at four longitudinal positions respectively at  $z/R_0 = 20, 21, 22, 24$ . The main difference between GD and BD cases

is about the length of the severely damaged zone ( $E^\dagger(t_0, z) < 0.5$  or  $d(t_0, z) > 0.5$  with  $d = 1 - E^\dagger$ ), according to our initial damage conditions defined in section 2.4. Depending on the initial level of damage, full re-endothelization is achieved between few hours (where  $d_0 < 0.1$ ) and 14 days (where  $d_0 = 0.99$ ) as seen in Figure 10 (c). The ranges of timescale of restoration of the EC layer, according to the degree of injury, is consistent with values reported in [12]. Endothelial regeneration in zones where  $d_0 > 0.5$  being longer because of the logistic dynamics, we observe in the BD that a large part of the initially injured zone is still significantly damaged ( $E^\dagger(t = 6\text{d}) < 0.5$ ) at  $t = 6$  days compared to the GD case, where a thin band centred on  $z/R_0 = 20$  still remains significantly damaged (Figure 10 (a)).

We assess the consequences of these two models of damage on the dynamics of vascular species below.

### 3.2.2 Functional properties of vSMCs

We discuss here the spatio-temporal evolution of functional properties of vSMCs linked with bioavailability of GFs and WSS stimuli [12]. Figure 11 presents in each row the time evolution of functional properties for GD and BD cases. The first two columns of plots show their isocontours

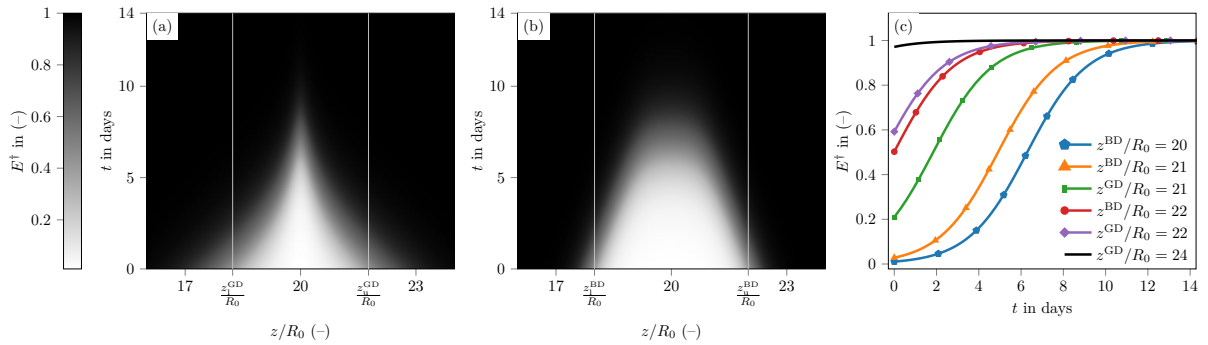


**Fig. 10:** Re-endothelization of the ECs in term of  $E^\dagger(t, z) = E(t, z)/E_{\max}(z)$ , the rescaled EC count by its maximal value at each compartment, in the first 14 days. For (a,b) plots,  $x$ -axis is the dimensionless longitudinal position  $z/R_0$  and  $y$ -axis is time in days. (c) Time evolution of ECs at several longitudinal position.

956 in  $(z, t)$  plane, with a dashed line where SFPs is 990  
 957 zero in order to show on/off switch or change of 991  
 958 property sign. The third column of plots shows 992  
 959 curves in time of the SFPs at relevant longitudinal 993  
 960 positions along the artery. 994

961 The first row of Figure 11 presents the intimal 995  
 962 dedifferentiation  $c_i(t, z)$  of cSMCs into sSMCs for 996  
 963 GD (a) and BD (b). The spatio-temporal evolu- 997  
 964 tion of  $c_i$  is globally the same for both damages 998  
 965 with a switch on at the centre of damaged zone 999  
 966 from the beginning of the simulation and a switch 1000  
 967 off around days 22 in this same region. In regions 1001  
 968 downstream the initial damages, and to a lesser 1002  
 969 extent upstream,  $c_i$  continue to be expressed (see 1003  
 970 contour of  $c_i = 0$  in dashed line in Figure 11 (a) 1004  
 971 and (b)) with even an increase in its intensity. In 1005  
 972 the damaged zones, the time interval where  $c_i$  is 1006  
 973 switch on, by the use of MMFs, and the  $c_i$  inten- 1007  
 974 sity are the same for both models of damage and 1008  
 975 1D case between 0 and 30 days (see Figure 11 (c)). 1009  
 976 The two differences between GD and BD can be 1010  
 977 seen in the length of the artery subject to pro- 1011  
 978 growth functional properties (greater in the BD 1012  
 979 case because of a strong damage more spread out) 1013  
 980 and in the dedifferentiation intensity downstream 1014  
 981 the damaged zones. The increase in dedifferentia- 1015  
 982 tion is stronger in the BD case than in GD case 1016  
 983 as seen in Figure 11 (c). 1017

984 The second row of Figure 11 presents for GD 1018  
 985 (a) and BD (b) the migration of vSMC within 1019  
 986 intima layer  $m_i(t, z)$ . Migration intensity and time 1020  
 987 interval are equivalent for both cases but the 1021  
 988 length of the artery subject to migration is greater 1022  
 989 in BD, due to the nature of the BD denudation

(see Figure 10). Note that unlike  $c_i$ , in any case 990  
 migration (which use MMFs) is not triggered out- 991  
 side of the injury areas, whether it be downstream 992  
 or upstream (see Figure 11 (a) and (b)). The 993  
 non-switch on outside damaged zones is mainly 994  
 due to the choice of threshold migration value 995  
 $t_m = 1.8$ , higher than threshold dedifferentiation 996  
 value  $t_c = 1.2$  (see [12] for parameter values). 997  
 Figure 11 (c) compares migration rates in 1D case, 998  
 GD and BD at  $z/R_0 = 20, 21$ . At  $z/R_0 = 20$ , all 999  
 cases are equivalent in intensity and duration of 1000  
 the expression of migration, starting in all cases on 1001  
 day 3.5. The only slight difference is the end time 1002  
 of migration, that occurs earlier in bidimensional 1003  
 simulations. 1004

The final row of Figure 11 concerns the 1005  
 turnover rate of sSMCs, *i.e.* proliferation minus 1006  
 apoptosis as  $r_i = p_i - a_i$ , for GD (g), BD (h) and 1007  
 a comparison of 1D case, GD and BD at positions 1008  
 $z/R_0 = 20, 22$  (i). As for migration and dedifferen- 1009  
 tiation processes, the main difference between GD 1010  
 and BD is about the length of the artery prone to 1011  
 cellular hyperplasia where  $r_i > 0$ , highlighted with 1012  
 an isocontour of  $r_i = 0$  in Figure 11 (g,h). The 1013  
 $r_i = 0$  contour highlights, from approximately 15 1014  
 days, the zone prone to hyperplasia and its motion 1015  
 downstream of the initial damage. This displace- 1016  
 ment is stronger with a higher intensity in BD case 1017  
 with  $r_i > 0.1$  after 25 days (see Figure 11 (h,i)). 1018  
 After 30 days, almost all the zone initially dam- 1019  
 aged ( $z/R_0 \in [19, 21]$ ) expresses negative turnover 1020  
 rates of sSMCs. Only the downstream zones have 1021  
 positive turnover rates (see Figure 11 (g,h,i)). 1022

As in the 1D case, during the first two weeks, the imbalance between cellular proliferation and apoptosis leads to onset of lesions (seen Figure 5). At  $z/R_0 = 20$ , the instants when we switch from cellular growth into cellular loss are in the GD case at  $t = 16$  days and in the BD case at  $t = 18$  days. Both instants appear before that of 1D case at  $t = 21$  days. In Figure 11 (i), we present the evolution of  $r_i$  in one downstream region of the initial damage at  $z/R_0 = 22$ . This region is slightly injured initially, *i.e.*  $d_0 \leq 0.5$  (Figure 10), yet we observe an increase of the functional property in both GD and BD cases, with a greater one for BD case. This increase in the turnover rate of sSMCs is at the origin of the lesion development observed downstream of the initially damaged zone, visible in Figure 5, and it is due to the low WSS exerted in this zone over this time interval (see Figures 8 and 9 for  $t \in [10, 30]$  days).

### 3.2.3 Dynamics of sSMCs

We show in Figure 12 the predicted sSMCs dynamics within intima and media layers between 0 and 100 days for the two considered cases. These dynamics presented in this section results directly from the spatio-temporal evolutions of their functional properties described above.

The first row of Figure 12 shows the intimal sSMCs dynamics through  $S_i^f(t, z)$ , the counts of SMCs  $S_i(t, z)$  divided by its initial-physiological compartmental count  $S_i^{\text{ph}}(z)$ . The two initial damages triggered a hyperplasia in the centre of the damaged zones at short timescale within  $t < 20$  days. Rapidly, the lesions resorbed in the central region as seen in Figure 12 (c). These two phases of narrowing and enlargement, seen in the 1D case, are driven by SFPs dynamics which itself is driven by GFs dynamics and WSS stimuli. Important intimal hyperplasia in the regions downstream of the initial damages ( $z/R_0 > 22$ ) is not seen in either GD or BD cases whereas SFPs prone to tissue growth are expressed, *e.g.* the turnover rates  $r_i^{\text{GD, BD}} > 0$  and dedifferentiation rates  $c_i^{\text{GD, BD}} > 0$ , which contribute to the definition of pathology-promoting zones. This lack of significant IH in these regions is due to the non-migration of cells from the media to the intima seen in Figures 11 (d,e,f). A further consequence

of the non-expression of cell migration is the prediction of medial hyperplasia in the downstream areas which we are now discussing.

The second row of Figure 12 shows the normalized media count of sSMCs  $S_m^f(t, z)$ . In both damages, we observe a spatio-temporal dynamics of a hyperplasia developing in the damaged zones at short timescale (within  $t < 20$  days) and then mainly moving downstream the initial damaged zones.

As described in [12], at short timescale, the formation of the lesion is due to the denudation of the endothelium which activates the functional properties pro-growth of vSMCs. The predicted intimal and medial hyperplasia phases in damaged zones are shorter and weaker than the one of 1D case (Figures 12 (c) and (f) at  $z/R_0 = 20$ ). As seen in Figure 11 (i) for the intimal turnover, this is provoked by a shorter interval prone to cellular proliferation with  $r_{i,m} > 0$ . Note that the intensity of medial hyperplasia is maximal in downstream regions where initial endothelial damage was slight, *i.e.*  $d_0 \leq 0.5$  (see Figure 10). The maxima of medial sSMCs are for GD  $S_m^{\text{f,max}}(t = 24.57\text{d}, z/R_0 = 20.59) = 10.89$  and for BD  $S_m^{\text{f,max}}(t = 52.28\text{d}, z/R_0 = 22.46) = 14.54$ .

The narrowing phases downstream the initial damage — discussed in section 3.1.1, for BD in  $z^{\text{BD}}/R_0 \in [22, 22.6]$  and for GD in  $z^{\text{BD}}/R_0 \in [22.2, 22.4]$  (see in Figure 4) — are the consequence of the spatio-temporal evolutions of sSMCs presented in this section. In both models of damage, the increase of  $r_i$  and switch on of  $c_i$  in the downstream region of the initial damage promote tissue growth and are due to the WSS distribution which have, because of the lesion development, values lower than the physiological one ( $\tau_w/\tau_w^{\text{ph}} < 1$ ) (see Figure 8 and 9). In that type of flow regions, it is known that production of GFs by ECs and permeability to plasma molecules are disturbed, which is called “*endothelial dysfunctions*” [16]. Our model succeeded in reproducing the characteristics of a pathology-promoting zone, with  $r_i > 0$  and  $c_i > 0$ , in both intima (see Figure 11) and media (data not shown), thanks to the multiple assumptions made at various spatial and temporal scales [12]. The only functional property not expressed in downstream regions is the migration. We has chosen a threshold value for migration of  $t_m = 1.8$  to fit experimental finding about cellular migration

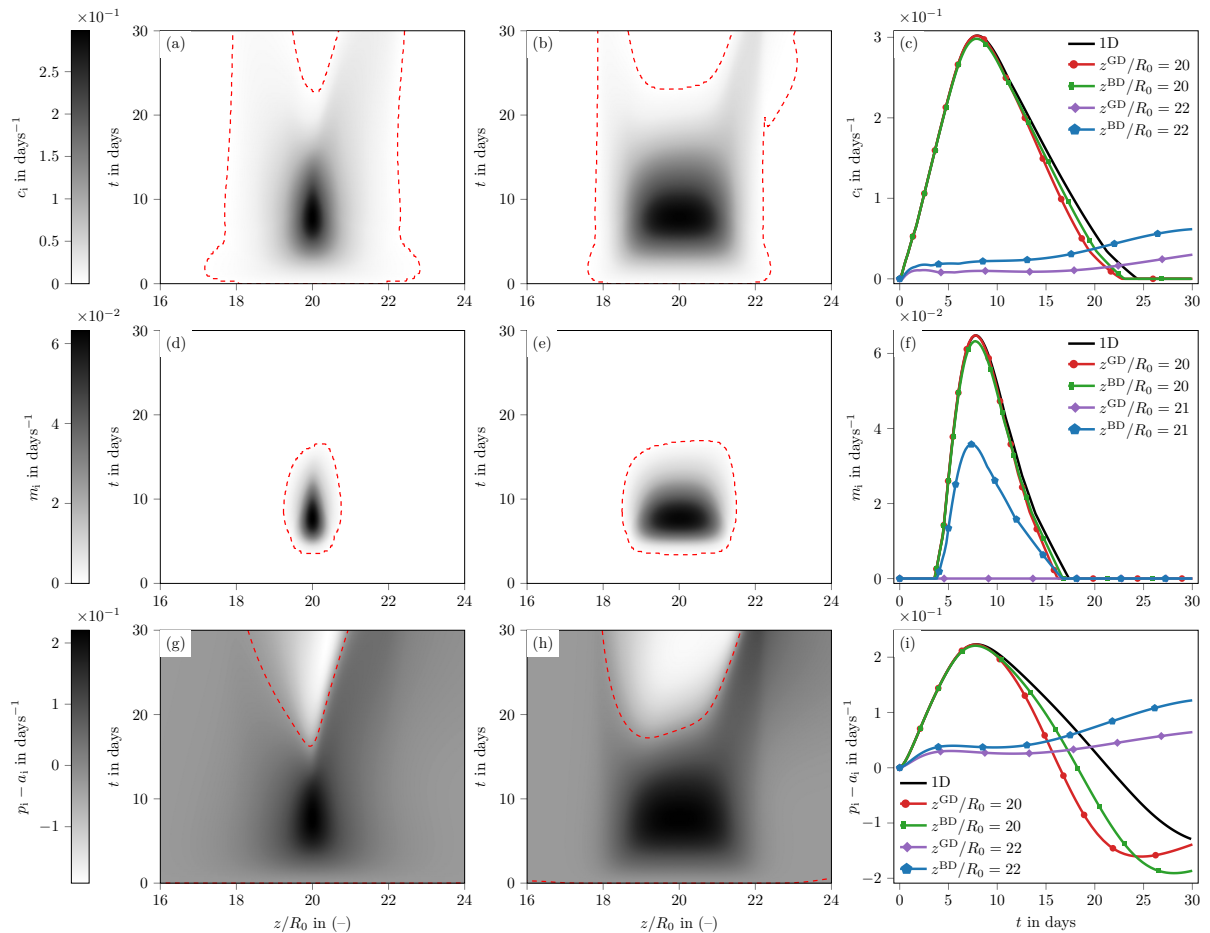


**Fig. 11:** Evolutions of the FPs of vSMCs in gaussian, bump and 1D case between 0 and 30 days. For (a,b,d,e,g,h) plots,  $x$ -axis is the dimensionless longitudinal position  $z/R_0$  and  $y$ -axis is time in days. (c,f,i) Time evolution of FPs at several longitudinal position. Intimal dedifferentiation rate of vSMCs  $c_i(t, z)$  in GD (a) and BD (b). Time evolution of  $c_i$  in 1D, GD and BD cases (c). Intimal migration rates of vSMCs  $m_i(t, z)$  in GD (d) and BD (e). Time evolution of  $m_i$  in 1D, GD and BD cases (f). Intimal turnover of sSMCs  $r_i(t, z)$  in GD (g) and BD (h). Time evolution of  $r_i$  in 1D, GD and BD cases (i).

1120 starting around  $t \in [2, 4]$  days [12]. Regarding 1134  
 1121 the absence of intimal hyperplasia in downstream 1135  
 1122 developing lesions, a inferior value will permit to 1136  
 1123 express this cellular functional property, *e.g.* the 1137  
 1124 value of  $t_m = 1.2$  has been tested and has permit- 1138  
 1125 ted to predict a intimal hyperplasia in downstream 1139  
 1126 regions in both type of damages [11]. 1140

1127 By comparing the predictions of the IH model 1141  
 1128 according to the two types of damage, we observe 1142  
 1129 a tissue growth strongly modulated by the mor- 1143  
 1130 phology of the stenosis. Indeed, we note that in the 1144  
 1131 presence of a stenosis having a smooth and diffuse 1145  
 1132 morphology, like that induced by GD at  $t = 20$  1144  
 1133 days (see Figure 5 (c)), the hyperplastic response

of the model downstream of this stenosis is less  
 than that produced by the initial disendotheliza-  
 tion. On the contrary, for a stenosis having a stiff  
 and focal morphology, such as that induced by  
 the BD at  $t = 20$  days (see Figure 5 (d)), the  
 hyperplastic response downstream of this steno-  
 sis is of a similar intensity to that induced by  
 disendothelization.

### 3.2.4 Composition of lesions

Figure 13 shows the spatio-temporal evolution of  
 the intimal layer composition in terms of the vol-  
 ume fraction  $\varphi_i(t, z)$  of vSMCs and ECM (collagen

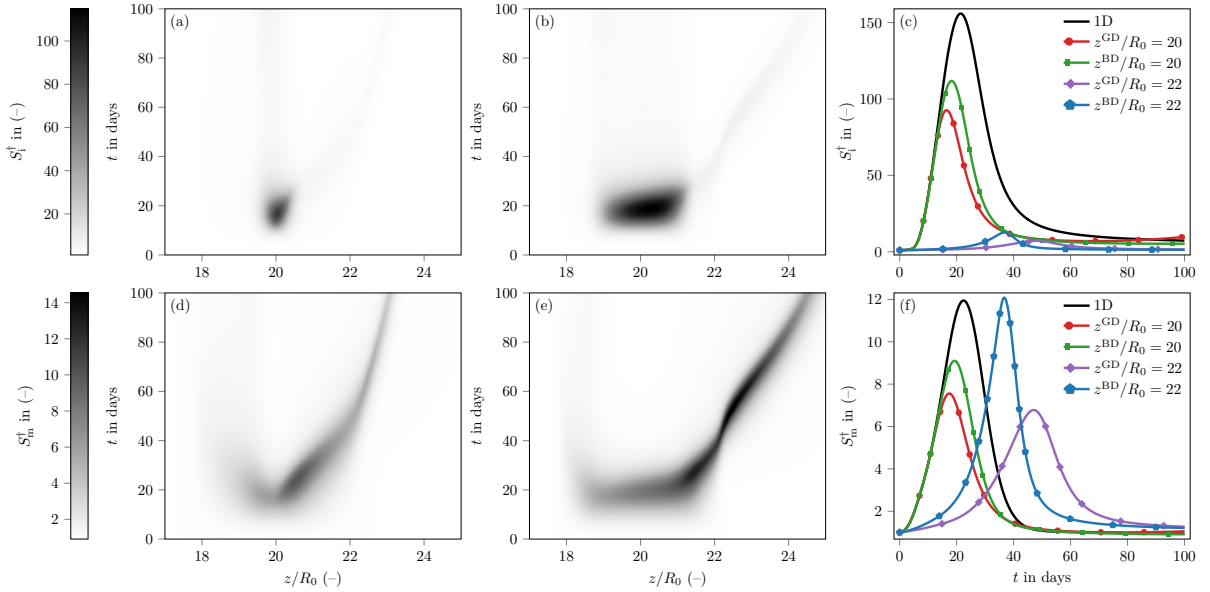


**Fig. 12:** Evolutions of intimal and medial rescaled sSMCs population,  $S_{i,m}^\dagger$ , in GD, BD and 1D case between 0 and 100 days. For (a,b,d,e) plots,  $x$ -axis is the dimensionless longitudinal position  $z/R_0$  and  $y$ -axis is time in days. (c,f) Time evolution of  $S_{i,m}^\dagger$  at several longitudinal positions.  $S_i^\dagger$  in GD (a) and BD (b). Time evolution of  $S_i^\dagger$  in 1D, GD and BD cases (c).  $S_m^\dagger$  in GD (d) and BD (e). Time evolution of  $S_m^\dagger$  in 1D, GD and BD cases (f).

1146 in our model) for the two models of damage. 1171  
 1147 From initial time until 12 months post-damage, 1172  
 1148 we present the overall evolution as well as tempo- 1173  
 1149 ral evolutions at several characteristic longitudinal 1174  
 1150 positions in Figures 13 (e,f) compared to 1D 1175  
 1151 test-case results. 1176

1152 For each initial disendothelization, respectively 1177  
 1153 in Figures 13 (a,c) for GD and in Figures 13 (b,d) 1178  
 1154 for BD, we follow the maturation process of the 1179  
 1155 lesion along the artery. As in our monodimensional 1180  
 1156 test-case, during the lesion formation, we observe 1181  
 1157 an intima layer that is more cellular than fibrous. 1182  
 1158 Over time and especially in the centre of the ini- 1183  
 1159 tially damaged zone ( $19 < z/R_0 < 21$ ), the intima 1184  
 1160 becomes more fibrous and less cellular. 1185

1161 In both damages at the centre of the damaged 1186  
 1162 zone ( $z/R_0 = 20$ ), during the first 20 days, the 1187  
 1163 dynamics of volume fraction obtained in axisym- 1188  
 1164 metric configuration is identical to that of 1D case 1189  
 1165 (see Figures 13 (e,f)). However, between 1 and 1190  
 1166 12 months, the maturation process of the lesion 1191  
 1167 is different between 1D and axisymmetric config- 1192  
 1168 uration in both damages. Despite these different 1193  
 1169 behaviours, after one year in the GD and BD 1194  
 1170 cases, the lesion in the centre of the injury has an 1195

equivalent composition to that of the 1D test-case 1171  
 and the experiments from the literature, *i.e.* 80% 1172  
 of ECM and 20 % of vSMCs [12].

Figure 13 informs also about the continuous 1173  
 downstream displacement of the lesion which is 1174  
 indicated by arrows in Figures 13 (a,b,c,d). At 1175  
 12 months, the developing intimal hyperplasia in 1176  
 GD and BD cases are respectively at  $z/R_0 \sim 24.8$  1177  
 and  $z/R_0 \sim 28$  (see Figures 13 (a,b)). Over the 1178  
 same duration of 12 months, BD case presents 1179  
 a higher continuous downstream displacement of 1180  
 the incipient lesion than the GD case. Thus, the 1181  
 displacement velocity is greater in the BD case 1182  
 compared to the GD case. During the first year 1183  
 post-damage, in both disendothelization models, 1184  
 the lesion displacement velocity decreases among 1185  
 time, *e.g.* during the first 100 days ( $\sim 3.3$  months), 1186  
 the maximum volume fraction of vSMCs moves in 1187  
 GD and BD cases respectively by  $3R_0$  and  $4.5R_0$ , 1188  
 while during the last 265 days ( $\sim 8.8$  months), the 1189  
 maximum moves in GD and BD cases respectively 1190  
 by  $1.83R_0$  and  $3.5R_0$  (see Figures 13 (a,b)). 1191

Downstream of the initial zone of damage, we 1192  
 find for the volume fraction of vSMCs an increase 1193  
 leading to a maximum then a decrease until the 1194  
 1195

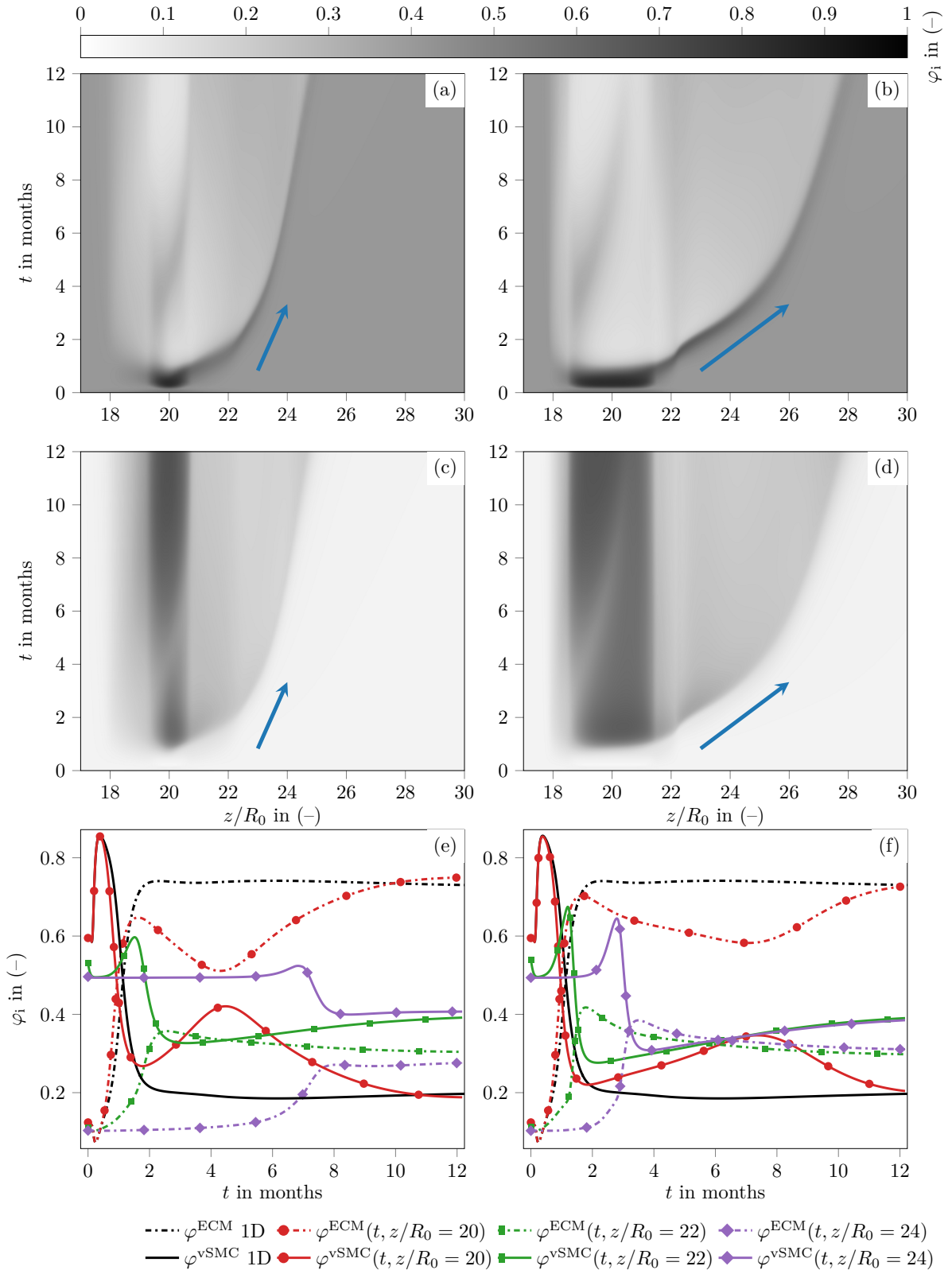


**Fig. 13:** Evolutions of intimal volume fractions  $\varphi_i(t, z)$  of vSMCs and ECM between 0 and 12 months. For (a,b,c,d) plots,  $x$ -axis is the dimensionless longitudinal position  $z/R_0$  and  $y$ -axis is time in months. (e,f) Time evolution of  $\varphi_i(t, z)$  at several longitudinal positions.  $\varphi_i^{\text{vSMC}}(t, z)$  in GD (a) and BD (b).  $\varphi_i^{\text{ECM}}(t, z)$  in GD (c) and BD (d). Time evolution of  $\varphi_i$  between 1D/GD cases (e) and between 1D/BD cases (f).

1196 stabilization of  $\varphi_i^{\text{vSMC}}$ . The inverse dynamics is 1245  
 1197 visible for  $\varphi_i^{\text{ECM}}$ . It is interesting to underline that 1246  
 1198 downstream of the initial damage, and contrary to 1247  
 1199 what occurs at the centre, the lesions in both types 1248  
 1200 of injury are all, after one year, more composed of 1249  
 1201 vSMCs than of ECM, *i.e.*  $\varphi_i^{\text{vSMC}}(t, z/R_0 \geq 22) >$  1250  
 1202  $\varphi_i^{\text{ECM}}(t, z/R_0 \geq 22)$ . This characteristic compo- 1251  
 1203 sition arises from an absence of strong intimal 1252  
 1204 hyperplasia at short timescale. Indeed, in order 1253  
 1205 to obtain a lesion mainly composed of collagen at 1254  
 1206 long timescale, it is essential that a strong prolifer- 1255  
 1207 ation of vSMCs be expressed. We notice that each 1256  
 1208 peak of  $\varphi^{\text{vSMC}}$  precedes a strong increase in the 1257  
 1209 volume fraction of collagen  $\varphi^{\text{ECM}}$ . This is particu- 1258  
 1210 larly clearly visible in axisymmetric configuration 1259  
 1211 for both damages in Figures 13 (e,f) at  $z/R_0 = 20$ . 1260

## 1212 4 Conclusion and perspectives 1262

1213 In the present work, we apply our multiscale 1264  
 1214 model of intimal hyperplasia to an axisymmet- 1265  
 1215 ric artery in which a steady hemodynamics is 1266  
 1216 considered. The spatio-temporal evolution of two 1267  
 1217 types of lesion has been simulated considering two 1268  
 1218 models of disendothelization. 1269

1219 By considering two models of damage, we 1270  
 1220 assess the influence of this initial condition on the 1271  
 1221 spatio-temporal evolution of the lesion. The two 1272  
 1222 damages, focal for the bump damage (BD), and 1273  
 1223 diffuse for the gaussian damage (GD), induce, in 1274  
 1224 the disendothelized zone, similar lesions in terms 1275  
 1225 of morphology and composition. In these central 1276  
 1226 zones, focal- or diffuse-type hyperplastic lesions 1277  
 1227 develop over a period of 20 days post-damage. 1278  
 1228 Then, these hyperplasia vanish and the lesions 1279  
 1229 become more and more fibrous. 1280

1230 According to all our comparisons of the 1D 1281  
 1231 and axisymmetric cases, the main results vali- 1282  
 1232 dating the model in 1D test-case are observed 1283  
 1233 in an axisymmetric artery at the centre of the 1284  
 1234 damaged zone. By this comparison, we ensure 1285  
 1235 the non-regression of the axisymmetric predic- 1286  
 1236 tion compared to the validated results in 1D [12]. 1287  
 1237 These main results found in the central damaged 1288  
 1238 zone of our axisymmetric artery ( $z/R_0 = 20$ ) 1289  
 1239 are: a short-lived intimal hyperplasia causing a 1290  
 1240 predominantly cellular lesion; long-term matura- 1291  
 1241 tion inducing a predominantly fibrous lesion with 1292  
 1242 80% of ECM and 20 % of vSMCs. However, due 1293  
 1243 to a more realistic geometrical configuration, the 1294  
 1244 dynamics predicted by the axisymmetric artery at 1295

$z/R_0 = 20$  is slightly different from that of the 1D  
 case.

After the 20<sup>th</sup> day, while the stenosis is max-  
 imal in the injured zones, our IH model predicts  
 a new hyperplastic development downstream of  
 the stenosis in BD and GD. This downstream  
 tissue growth is induced by zones of low WSS  
 downstream of the stenosis caused by initial dis-  
 endothelization. Our two simulations succeed to  
 capture accurately the downstream development  
 of lesion thanks to the automatic remodelling  
 criteria which permit to overcome constant remod-  
 elling intervals by considering remodeling frequen-  
 cies dependent on lesion dynamics. Macroscopi-  
 cally, the sensitivity of the model to pathology-  
 promoting and pathology-protective zones is qual-  
 itatively consistent with experimental results [15,  
 20]. This consistency only results from the mod-  
 elling of biological and biochemical hypotheses  
 made at the cellular scale [12].

As seen in our two simulations, the matu-  
 ration process of IH lesions is well captured by  
 our modelling because it is a direct consequence  
 of concurrency of three modeled mechanisms of  
 promotion/inhibition of IH [15], production of col-  
 lagen fiber by sSMCs and arterial remodeling.  
 At short timescale, the model predicts an incipi-  
 ent stenosis mainly cellular. Thus, because of the  
 growing stenosis and narrowing remodeling events  
 in the injured zone, the WSS increases which  
 inhibit cellular growth over time. At the same  
 time, downstream the damaged zone, the WSS  
 decrease below physiological value which promote  
 cellular growth. As we consider a loose coupling  
 between hemodynamics and arterial remodeling,  
 in both cell decrease or growth phases, remodeling  
 events of the arterial lumen permit to modulate  
 biochemical, cellular and fibrotic dynamics.

Nevertheless, we could not quantitatively vali-  
 date the predictions of our model in terms of  
 downstream lesion displacement resulting from  
 the consistency of areas of high and low levels  
 of WSS. Indeed, to our knowledge, there are no  
 experimental data on the spatio-temporal evolu-  
 tion of intimal hyperplasia lesion that we could  
 transpose to the *in silico* experiences of idealized  
 arteries undergoing disendothelizations proposed  
 in this work.

Lesion displacement is predicted in both dam-  
 ages following the appearance of lesions in the  
 initially disendothelized zones. The lesion moves

continuously downstream with a speed of movement influenced mainly by the morphology of the stenosis. This displacement is self-sustained over time by both the high WSS levels in the zone of maximum stenosis promoting tissue decrease on the one hand, and on the other hand, downstream of the stenosis by the low WSS promoting tissue growth.

According to the simulations presented in this article, the initial damage plays a central role in the genesis of intimal hyperplasia, while the local WSS controls the spatio-temporal evolution of the lesion after its onset. Thus, we found that the morphology of the stenosis strongly influences the spatial variation of WSS, which in turn affects the dynamics of the tissue growth: a smooth and diffuse stenosis morphology, as seen during GD lesion development, results in less hyperplastic response than stiff and focal stenosis morphology, induced during the BD lesion development.

Our study opens the following perspectives by suggesting possible improvements of the model.

Firstly, given the importance of endothelial damage and regeneration on lesion development, the model could be enriched by taking into account hemodynamical influence of WSS on the dynamics of endothelial cells as reviewed in [3, 14]. This improvement is totally feasible in our modelling by considering a WSS-dependent proliferation rate in our equation for ECs dynamics which may slow or accelerate proliferation depending on flow conditions. As the process of regeneration of ECs drives the genesis of IH, we assume that this improvement of the model could be of great interest.

Given the good agreement of (a) our axisymmetric results in the central damage zone compared to our 1D case validated, and (b) the prediction of the model regarding the concept of pathology promotion and protection zones, new in silico experiments are called for to provide insights of IH development all along the arterial tree. These experiments will have to consider different flow regimes, geometrical configurations and initial structures of the arterial wall regarding the type of artery. The latter point will be challenging as geometrical and cellular properties along the arterial tree are scarce in literature.

## 5 Acknowledgments

Numerical simulations were carried out using the facilities of the PMCS2I of École Centrale de Lyon. We gratefully thank the entire staff of PMCS2I for the technical support, and especially Laurent Pouilloux for his infallible help.

## A Reproducibility data, computational costs and sensitivity analysis

For the sake of further studies, we present in this section the reproducibility data in Tables 2 and 3 and the computational costs of our two disendothelization models simulations.

Numerical simulations were carried out in parallel on twelve processors of the PMCS2I of École Centrale de Lyon. The simulations lasted 1.17 days and 3.96 days respectively for the bump damage (BD) and the gaussian damage (GD). The axisymmetric artery geometry is more CPU time consuming than the one in monodimensional artery. For information, the computational cost of 1D test-case in [12] is about 0.2 minutes.

Because of the prohibitive computational cost of the axisymmetric cases compared to the 1D test-case, we perform a sensitivity study of the parameters of our model only in the 1D configuration. In [11, section 6.2], we propose a qualitative and quantitative exploration of the parameter space of our model using a methodology that nests two Global Sensitivity Analysis (GSA) methods. The realization of such sensitivity analysis methods in axisymmetric geometry could not have been achieved because of its computational cost.

## B Mesh convergence study

In this section, we present the convergence studies used to set relevant mesh parameters for the presented simulations. These parameters define the meshes of the luminal domain linked to CFD and of the parietal domain linked to the model of intimal hyperplasia. An illustration of the mesh parameters of domains is proposed in Figure 14 (d). The convergence studies were carried out on the gaussian damage (GD). The fixed and variable parameters of each study are presented in Table 4.



**Table 1:** OpenFOAM boundary conditions used at boundaries of the luminal axisymmetric domain  $\Omega_1$  shown in Figure 1. parabolicInletVelocity is custom boundary condition of a Poiseuille velocity profile from (2a).

	$u$	$p$
Inlet $\Gamma_1^{\text{in}}$	parabolicInletVelocity	zeroGradient
Outlet $\Gamma_1^{\text{out}}$	pressureInletOutletVelocity	fixedValue 0
Endothelium $\Gamma_1^e$	fixedValue (0 0 0)	zeroGradient
Wedges $\Gamma_1^{w0,1}$	wedge	wedge

**Table 2:** Numerical schemes of OpenFOAM used for spatial and temporal discretisation of equations (1).

ddtSchemes	gradSchemes	divSchemes	laplacianSchemes	interpolationSchemes	snGradSchemes
steadyState	leastSquares	bounded Gauss linearUpwind grad(U)	Gauss linear corrected	linear	corrected

1388 A first study, shown in Figure 14 (a), impose  
 1389 conformed meshes between luminal and parietal  
 1390 meshes to choose the relevant discretization in the  
 1391 damaged zone of parietal mesh. This figure shows,  
 1392 as a function of the number of parietal mesh points  
 1393 in the central zone of the GD case,  $N_{\text{TG}}^M$  (see  
 1394 Figure 14 (d)), the relative error of luminal radius  
 1395 at  $t = 60$  days, *i.e.*  $R_1(z, t = 60\text{d})$ , based on a finer  
 1396 mesh which has  $N_{\text{TG}}^M = 1301$ . From this study, we  
 1397 choose  $N_{\text{TG}}^M = 1001$ .

1398 As the whole coupling between hemodynamics  
 1399 and tissue growth is based on the WSS distribu-  
 1400 tion, and regarding the strong influence of WSS  
 1401 on vascular species dynamics (see Figure 12), the  
 1402 most limiting factor for an accurate simulation  
 1403 of a spatio-temporal lesion evolution is the WSS  
 1404 computation. The more the hemodynamics will be  
 1405 finely resolved in the near endothelium region, the  
 1406 more precise the WSS will be obtained, within the  
 1407 feasible simulation limit.

1408 In order to evaluate the influence of the numer-  
 1409 ical resolution of hemodynamics in axisymmetric  
 1410 configuration, two parameters of the luminal mesh  
 1411 were tested: discretization in the radial direction  
 1412 and discretization in the longitudinal direction.

1413 Imposing a constant radial compression of the  
 1414 luminal mesh with a thickness of the near endothe-  
 1415 lium cell of  $\Delta_y = 1 \times 10^{-5}$  m, we study the  
 1416 influence of the number of points  $N_y$  and  $N_z^M$   
 1417 respectively in Figure 14 (b) and (c). In Figure  
 1418 14 (b), we observe a strong dependence of the  
 1419 number of points of mesh in the radial direction,  
 1420 with constant radial compression. From this study,  
 1421 we choose  $N_y = 51$ . Fixing  $N_{\text{TG}}^M = 1000$ , the  
 1422 Figure 14 (c) shows the influence of the increase  
 1423 in the longitudinal discretization of the luminal  
 1424 mesh on the relative errors of the luminal radius  
 1425 at  $t = 60$  days, based on the finer luminal mesh  
 1426 with  $N_z^M/N_{\text{TG}}^M = 8$ . From this study, we impose  
 1427 the ratio  $N_z^M/N_{\text{TG}}^M = 7$ .

**Table 3:** Definitions, values and units of the parameters of the model in a axisymmetric artery configuration. The parameters are grouped in several topics sections. For other parameters not specified in this table, refer to Tables in [12]. All the parameter values displayed in this table have been chosen. For mesh parameters, an illustration of meshes is shown in Figure 14 (d).

Constant	Description	Value	Units
Geometry of the axisymmetric artery			
$R_0$	Initial luminal radius	$4 \times 10^{-3}$	m
$R_{ext}$	External wall radius	$4.5 \times 10^{-3}$	m
$L_I$	Arterial inlet zone length	$15 R_0$	m
$L_M$	Arterial central zone length	$15 R_0$	m
$L_O$	Arterial outlet zone length	$15 R_0$	m
Others parameters see [12, Table 1]			
Models of disendothelization			
$z_G$	Center of the damaged zone	$8 \times 10^{-2}$	m
$\sigma_G$	Damage length control parameter	$6 \times 10^{-3}$	m
$z_1^{BD}$	Lower limit of damage	$7.2 \times 10^{-2}$	m
$z_u^{BD}$	Upper limit of damage	$8.8 \times 10^{-2}$	m
$\delta_z$	Transition length parameter	$2 \times 10^{-3}$	m
Hemodynamics			
$Re_0$	Initial Reynolds number	$3.0 \times 10^2$	–
Others parameters see [12, Table 1]			
Intimal hyperplasia model			
$l_M$	Half smoothing distance of the MMF	$5 \times 10^{-2}$	–
Others parameters see [12, Table 1]			
Temporal integration			
$t_0$	Initial time	0	day
$t_f$	Final time	365	day
$d_0$	Maximum initial damage parameter	$9.9 \times 10^{-1}$	–
$\mathbf{y}_0$	Initial conditions	‡	–
$\mathbf{h}_0$	History conditions	‡	–
Others parameters see [12, Table 1]			
Parietal mesh			
$N_{TG}^{I,O}$	Number of parietal point in inlet and outlet arterial zones of length $L_{I,O}$	2	–
$N_{TG}^M$	Number of parietal point in the central arterial zone of length $L_M$	1001	–
$N_{TG}$	Total number of parietal compartments	1002	–
Luminal mesh			
$N_z^{I,O}$	Number of luminal point in the longitudinal direction at inlet/outlet arterial zones of length $L_{I,O}$	401	–
$N_z^M$	Number of luminal point in the longitudinal direction at the central arterial zone of length $L_M$	7000	–
$N_y$	Number of luminal point in the radial direction.	51	–
$\Delta_y$	Thickness of the near endothelium cell	$2 \times 10^{-5}$	m
$N^{cell}$	Total number of cells in the luminal mesh	389950	–
CFD boundary condition			
$u_{max}$	Maximal velocity at inlet	$2.45 \times 10^{-1}$	$m s^{-1}$
$R_{1,in}$	Inlet radius	$4 \times 10^{-3}$	m
$p_{out}$	Outlet pressure	0	Pa
CFD resolution parameters			
$N_{nnO}$	Number of SIMPLE explicit non-orthogonal correction	4	–
$p^r$	Pressure residual tolerance	$1 \times 10^{-6}$	–
$\mathbf{u}^r$	Velocity residual tolerance	$1 \times 10^{-6}$	–
$N_{max}$	Maximal number of SIMPLE iterations	1000	–
$\alpha_u^e$	Velocity equation relaxation factor	0.7	–
$\alpha_p^e$	Pressure equation relaxation factor	0.7	–
$\alpha_u^f$	Velocity field relaxation factor	1	–
$\alpha_p^f$	Pressure field relaxation factor	0.3	–

‡ Calculated from volume fractions of [12, Table 4]. Initial conditions and histories are functions of the volumes of compartments.

**Table 4:** Summary of the parameters of the luminal and parietal meshes in the three convergence studies proposed in Figure 14. For an illustration of the construction of luminal and parietal meshes from these parameters, see Figure 14 (d).

Fixed parameters	Variable parameters
Conform meshes case (see Figure 14 (a))	
$N_y = 31$ , $\Delta_y = 2 \times 10^{-5}$ m, $N_z^{I,O} = 401$ , $N_{TG}^{I,O} = 2$ ,	$N_{TG}^M \in [201, 1301]$ and $N_z^M = N_{TG}^M$
Variation in the radial direction for luminal mesh (see Figure 14 (b))	
$N_z^M = 1000$ , $N_z^{I,O} = 201$ , $\Delta_y = 1 \times 10^{-5}$ m, $N_{TG}^{I,O} = 2$ , $N_{TG}^M = 1000$	$N_y \in [11, 51]$
Variation in the longitudinal direction for luminal mesh (see Figure 14 (c))	
$N_z^{I,O} = 201$ , $N_y = 32$ , $\Delta_y = 1 \times 10^{-5}$ m, $N_{TG}^{I,O} = 2$ , $N_{TG}^M = 1000$	$N_z \in [1000, 7000]$

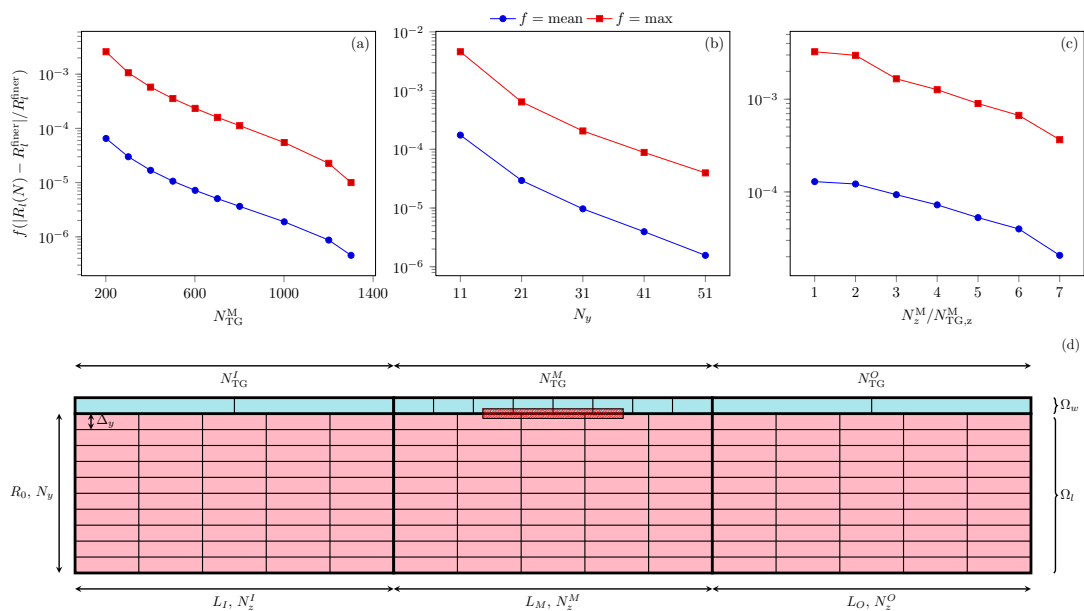


**Fig. 14:** Means and maximums of the relative error based on luminal radius at  $t = 60$  days with respect to the finer mesh in the gaussian damage. The fixed and variable parameters of each study are shown in Table 4. (a) Relative errors as a function of the number of points in the longitudinal direction in the central zone  $N_z^M$ . The finer mesh has  $N_z^M = 1301$  points. This study impose conform meshes between luminal and parietal domains. (b) Relative errors as a function of the number of points in the radial direction on the luminal mesh  $N_y$ . The finer mesh has  $N_y = 51$  points. This study impose constant radial compression of the luminal mesh. (c) Relative errors as a function of the ratio between the number of longitudinal points of luminal and parietal meshes for  $N_{TG}^M = 1000$ . (d) Illustration in the plane of symmetry of the artery of the meshes in the luminal and parietal domains with the various mesh parameters considered. A hatched rectangle with red lines shows the initially damaged zone limited.

## References

- [1] V. Calvez, J.G. Houot, N. Meunier, A. Raoult, and G. Rusnakova. Mathematical and numerical modeling of early atherosclerotic lesions. *ESAIM: Proc.*, 30:1–14, 2010. doi: 10.1051/proc/2010002.
- [2] A. Carrel and C.C. Guthrie. Results of the biterminal transplantation of veins. *The American Journal of the Medical Sciences*, 132:415–422, 1906.
- [3] D.A. Chistiakov, A.N. Orekhov, and Y.V. Bobryshev. Effects of shear stress on endothelial cells: go with the flow. *Acta Physiologica*, 219(2):382–408, 2016. doi: 10.1111/apha.12725.
- [4] M. Cilla, E. Peña, and M.A. Martínez. Mathematical modelling of atheroma plaque formation and development in coronary arteries. *Journal of the Royal Society, Interface*, 11 90: 20130866, 2014.
- [5] A. Corti, C. Chiastra, M. Colombo, M. Garbey, F. Migliavacca, and S. Casarin. A fully coupled computational fluid dynamics — agent-based model of atherosclerotic plaque development: Multiscale modeling framework and parameter sensitivity analysis. *Computers in Biology and Medicine*, 118: 103623, 2020. doi: 10.1016/j.compbimed.2020.103623.
- [6] F. Donadoni, C. Pichardo-Almarza, M. Bartlett, A. Dardik, S. Homer-Vanniasinkam, and V. Díaz-Zuccarini. Patient-specific, multi-scale modeling of neointimal hyperplasia in vein grafts. *Frontiers in Physiology*, 8:226, 2017. doi: 10.3389/fphys.2017.00226.
- [7] J. Escuer, M.A. Martínez, S. McGinty, and E. Peña. Mathematical modelling of the restenosis process after stent implantation. *Journal of The Royal Society Interface*, 16 (157):20190313, 2019. doi: 10.1098/rsif.2019.0313.
- [8] M.H. Friedman, G.M. Hutchins, C. Brent Bargeron, O.J. Deters, and F.F. Mark. Correlation between intimal thickness and fluid shear in human arteries. *Atherosclerosis*, 39(3):425–436, 1981. doi: 10.1016/0021-9150(81)90027-7.
- [9] C. Geuzaine and J.F. Remacle. Gmsh: A 3-D finite element mesh generator with built-in pre- and post-processing facilities. *International Journal for Numerical Methods in Engineering*, 79(11):1309–1331, 2009. doi: 10.1002/nme.2579.
- [10] M.E. Goodman, X.Y. Luo, and N.A. Hill. Mathematical model on the feedback between wall shear stress and intimal hyperplasia. *International Journal of Applied Mechanics*, 8(7), 2016.
- [11] J. Jansen. *Modélisation et simulation de l’écoulement hémodynamique couplé à la croissance tissulaire de l’endofibrose artérielle dans l’artère iliaque*. PhD thesis, Université de Lyon, 2021.
- [12] J. Jansen, X. Escriva, F.S. Godeferd, and P. Feugier. Multiscale bio-chemo-mechanical model of intimal hyperplasia. *Biomechanics and Modeling in Mechanobiology*, 21:709–734, 2022. doi: 10.1007/s10237-022-01558-5.
- [13] R. Khosravi, A.B. Ramachandra, J.M. Szafron, D.E. Schiavazzi, C.K. Breuer, and J.D. Humphrey. A computational bio-chemo-mechanical model of in vivo tissue-engineered vascular graft development. *Integrative Biology*, 12(3):47–63, 2020. doi: 10.1093/intbio/zyaa004.
- [14] Y.S.J. Li, J.H. Haga, and S. Chien. Molecular basis of the effects of shear stress on vascular endothelial cells. *Journal of Biomechanics*, 38(10):1949–1971, 2005. doi: 10.1016/j.jbiomech.2004.09.030.
- [15] V. Peiffer, S.J. Sherwin, and P.D. Weinberg. Does low and oscillatory wall shear stress correlate spatially with early atherosclerosis? a systematic review. *Cardiovascular Research*, 99(2):242–250, 2013. doi: 10.1093/cvr/cvt044.

- 1515 [16] J. Qiu, Y. Zheng, J. Hu, D. Liao,  
1516 H. Gregersen, X. Deng, Y. Fan, and G Wang.  
1517 Biomechanical regulation of vascular smooth  
1518 muscle cell functions: from *in vitro* to *in vivo*  
1519 understanding. *Journal of The Royal Soci-*  
1520 *ety Interface*, 11(90):20130852, 2014. doi:  
1521 10.1098/rsif.2013.0852.
- 1522 [17] L.F. Shampine and S. Thompson. *Numeri-*  
1523 *cal Solution of Delay Differential Equations*,  
1524 pages 1–27. 2009. doi: 10.1007/  
1525 978-0-387-85595-0\_9.
- 1526 [18] V.M. Subbotin. Analysis of arterial intimal  
1527 hyperplasia: review and hypothesis. *Theoreti-*  
1528 *cal Biology and Medical Modelling*, 4(1), 2007.  
1529 doi: 10.1186/1742-4682-4-41.
- 1530 [19] The OpenFOAM Foundation. *OpenFOAM*  
1531 *v5 User Guide*. OpenCFD Ltd., 5.0 edition,  
1532 2017.
- 1533 [20] J.J. Wentzel, F.J.H. Gijzen, N. Stergiopoulos,  
1534 P.W. Serruys, C.J. Slager, and R. Krams.  
1535 Shear stress, vascular remodeling and neoin-  
1536 timal formation. *Journal of Biomechan-*  
1537 *ics*, 36(5):681–688, 2003. doi: 10.1016/  
1538 S0021-9290(02)00446-3.